



# **NAVAL POSTGRADUATE SCHOOL**

**MONTEREY, CALIFORNIA**

## **THESIS**

**EFFECT OF ANNEALING ON THE PASSIVE FILM  
STABILITY AND CORROSION RESISTANCE OF NEW  
FAMILIIES OF IRON-BASED AMORPHOUS METALS**

by

Timothy Omlor

June 2011

Thesis Co-Advisors:

Joseph Farmer  
Luke Brewer

**Approved for public release; distribution is unlimited**

THIS PAGE INTENTIONALLY LEFT BLANK

<b>REPORT DOCUMENTATION PAGE</b>			<i>Form Approved OMB No. 0704-0188</i>	
Public reporting burden for this collection of information is estimated to average 1 hour per response, including the time for reviewing instruction, searching existing data sources, gathering and maintaining the data needed, and completing and reviewing the collection of information. Send comments regarding this burden estimate or any other aspect of this collection of information, including suggestions for reducing this burden, to Washington headquarters Services, Directorate for Information Operations and Reports, 1215 Jefferson Davis Highway, Suite 1204, Arlington, VA 22202-4302, and to the Office of Management and Budget, Paperwork Reduction Project (0704-0188) Washington DC 20503.				
<b>1. AGENCY USE ONLY (Leave blank)</b>		<b>2. REPORT DATE</b> June 2011	<b>3. REPORT TYPE AND DATES COVERED</b> Master's Thesis	
<b>4. TITLE AND SUBTITLE</b> Effect of Annealing on the Passive Film Stability and Corrosion Resistance of New Families of Iron-Based Amorphous Metals			<b>5. FUNDING NUMBERS</b>	
<b>6. AUTHOR(S)</b> ENS Timothy Omlor				
<b>7. PERFORMING ORGANIZATION NAME(S) AND ADDRESS(ES)</b> Naval Postgraduate School Monterey, CA 93943-5000			<b>8. PERFORMING ORGANIZATION REPORT NUMBER</b>	
<b>9. SPONSORING /MONITORING AGENCY NAME(S) AND ADDRESS(ES)</b> N/A			<b>10. SPONSORING/MONITORING AGENCY REPORT NUMBER</b>	
<b>11. SUPPLEMENTARY NOTES</b> The views expressed in this thesis are those of the author and do not reflect the official policy or position of the Department of Defense or the U.S. Government. IRB Protocol number ____N/A____.				
<b>12a. DISTRIBUTION / AVAILABILITY STATEMENT</b> Approved for public release; distribution is unlimited			<b>12b. DISTRIBUTION CODE</b> A	
<b>13. ABSTRACT (maximum 200 words)</b>  Iron-based amorphous metals have incredible strength and hardness, and with the addition of alloying constituents, can also be formulated to have exceptional corrosion resistance. Compositions of several iron-based amorphous metals have been published, including several with very good corrosion resistance. The benefits of chromium, molybdenum, and tungsten on corrosion resistance has been previously studied and documented, however little is known about other alloying constituents and their effect upon devitrification and corrosion resistance. The compositions explored in this thesis research are the SAM40 base alloy and variations including systematic additions of nickel, yttrium, and titanium. Nickel is added to improve both mechanical properties and corrosion resistance. Yttrium is added to lower the critical cooling rate, thereby making the metallic glass easier to create and more stable once formed, thus improving the corrosion resistance. Adding titanium will enable the formation of an extremely stable protective titanium oxide film on the alloy's surface, which could enhance the corrosion resistance. Through x-ray diffraction and corrosion analysis, the effects of these alloy additions on the devitrification and corrosion resistance of this new class of amorphous metals have be quantified.				
<b>14. SUBJECT TERMS</b> Bulk Metallic Glass, Amorphous, Devitrification,			<b>15. NUMBER OF PAGES</b> 89	
			<b>16. PRICE CODE</b>	
<b>17. SECURITY CLASSIFICATION OF REPORT</b> Unclassified	<b>18. SECURITY CLASSIFICATION OF THIS PAGE</b> Unclassified	<b>19. SECURITY CLASSIFICATION OF ABSTRACT</b> Unclassified	<b>20. LIMITATION OF ABSTRACT</b> UU	

NSN 7540-01-280-5500

Standard Form 298 (Rev. 2-89)  
Prescribed by ANSI Std. Z39-18

THIS PAGE INTENTIONALLY LEFT BLANK

**Approved for public release; distribution is unlimited**

**EFFECT OF ANNEALING ON THE PASSIVE FILM STABILITY AND  
CORROSION RESISTANCE OF NEW FAMILIES OF IRON-BASED  
AMORPHOUS METALS**

Timothy J. Omlor  
Ensign, United States Navy  
B.S. in Mechanical Engineering, United States Naval Academy, 2010

Submitted in partial fulfillment of the  
requirements for the degree of

**MASTER OF SCIENCE IN MECHANICAL ENGINEERING**

from the

**NAVAL POSTGRADUATE SCHOOL  
June 2011**

Author: Timothy J. Omlor

Approved by: Joseph Farmer  
Thesis Co-Advisor

Luke Brewer  
Thesis Co-Advisor

Knox Millsaps, PhD  
Chair, Department of Mechanical and Aerospace Engineering

THIS PAGE INTENTIONALLY LEFT BLANK

## **ABSTRACT**

Iron-based amorphous metals have incredible strength and hardness, and with the addition of alloying constituents, can also be formulated to have exceptional corrosion resistance. Compositions of several iron-based amorphous metals have been published, including several with very good corrosion resistance. The benefits of chromium, molybdenum, and tungsten on corrosion resistance has been previously studied and documented, however little is known about other alloying constituents and their effect upon devitrification and corrosion resistance. The compositions explored in this thesis research are the SAM40 base alloy and variations including systematic additions of nickel, yttrium, and titanium. Nickel is added to improve both mechanical properties and corrosion resistance. Yttrium is added to lower the critical cooling rate, thereby making the metallic glass easier to create and more stable once formed, thus improving the corrosion resistance. Adding titanium will enable the formation of an extremely stable protective titanium oxide film on the alloy's surface, which could enhance the corrosion resistance. Through x-ray diffraction and corrosion analysis, the effects of these alloy additions on the devitrification and corrosion resistance of this new class of amorphous metals have been quantified.

THIS PAGE INTENTIONALLY LEFT BLANK



## TABLE OF CONTENTS

<b>I.</b>	<b>INTRODUCTION.....</b>	<b>1</b>
<b>A.</b>	<b>AMORPHOUS METALS AND BULK METALLIC GLASSES .....</b>	<b>1</b>
<b>B.</b>	<b>PROCESSING OF AMORPHOUS METALS.....</b>	<b>2</b>
<b>C.</b>	<b>HISTORY AND BACKGROUND .....</b>	<b>4</b>
<b>D.</b>	<b>PRACTICAL IMPLEMENTATION OF BMG .....</b>	<b>4</b>
1.	Shipboard Use .....	5
2.	Spent Nuclear Fuel Storage.....	5
<b>II.</b>	<b>EXPERIMENTAL HYPOTHESES.....</b>	<b>7</b>
<b>A.</b>	<b>NICKEL ADDITION .....</b>	<b>7</b>
<b>B.</b>	<b>YTTRIUM ADDITION.....</b>	<b>7</b>
<b>C.</b>	<b>TITANIUM ADDITION .....</b>	<b>8</b>
<b>III.</b>	<b>COMPOSITIONAL CORROSION CHARACTERISICS.....</b>	<b>9</b>
<b>A.</b>	<b>EMPIRICAL METHODS USED IN DESIGNING ALLOYS FOR CORROSION RESISTANCE .....</b>	<b>9</b>
1.	Pitting Resistance Equivalence Number .....	9
2.	Pourbaix Diagrams .....	10
<b>IV.</b>	<b>EXPERIMENTAL DESIGN.....</b>	<b>13</b>
<b>A.</b>	<b>COMPOSITION OF SAM40 BASE ALLOY AND ITS DERIVATIVES.....</b>	<b>13</b>
<b>B.</b>	<b>ALLOY AND HEAT TREATMENT TEMPERATURE SELECTION ..</b>	<b>14</b>
<b>C.</b>	<b>HEAT TREATMENT .....</b>	<b>15</b>
1.	Argon Purged Furnace .....	15
2.	Sandia Argon Purged Furnace .....	16
3.	Vacuum Furnace .....	17
<b>D.</b>	<b>X-RAY DIFFRACTION SETUP AND PROCEDURE.....</b>	<b>17</b>
<b>E.</b>	<b>CYCLIC POLARIZATION SETUP AND PROCEDURE.....</b>	<b>19</b>
<b>V.</b>	<b>EXPERIMENTAL RESULTS.....</b>	<b>21</b>
<b>A.</b>	<b>STRUCTURAL CHARACTERIZATION OF MELT-SPUN RIBBONS.....</b>	<b>21</b>
1.	SAM40 Base Alloy.....	21
2.	SAM1X3 and SAM1X7 (Nickel Addition).....	21
3.	SAM3X3 and SAM3X7 (Yttrium Addition).....	27
4.	SAM4X3 and SAM4X7 (Titanium Addition).....	27
5.	Summary of X-ray Diffraction Results .....	28
<b>B.</b>	<b>ELECTROCHEMICAL CORROSION ANALYSIS OF MELT SPUN RIBBONS.....</b>	<b>29</b>
1.	Studies of SAM40 Base Alloy .....	29
2.	Studies of SAM1X3 and SAM1X7 (Nickel Addition) .....	30
3.	Studies of SAM3X3 and SAM3X7 (Yttrium Addition) .....	33
4.	Studies of SAM4X3 and SAM4X7 (Titanium Addition) .....	36

5.	Summary of Electrochemical Results .....	38
VI.	CONCLUSIONS .....	43
VII.	RECOMMENDATIONS FOR FUTURE RESEARCH.....	45
	LIST OF REFERENCES .....	47
	APPENDIX.....	49
	INITIAL DISTRIBUTION LIST .....	71

## LIST OF FIGURES

Figure 1.	Melt spinning ejects molten metal onto a spinning cooled copper wheel. ....	3
Figure 2.	Overlaid Pourbaix Diagram of SAM40. ....	11
Figure 3.	Photograph showing the copper test tube connected to the vacuum/argon tubing inside the furnace. ....	15
Figure 4.	Photograph of the assembled argon purged furnace. The vacuum pump is seen below the counter. ....	16
Figure 5.	Photograph of x-ray diffractometer. ....	18
Figure 6.	Photograph of melt-spun ribbons mounted on glass slide for an XRD scan. ..	19
Figure 7.	Photograph of the cyclic polarization test apparatus. ....	20
Figure 8.	SAM 40 XRD scan at multiple temperatures. ....	21
Figure 9.	Overlay of SAM1X3 XRD scans as cast, heat treated to 400°C, and heat treated to 700°C. ....	22
Figure 10.	Plot of XRD peaks of possible phases in SAM1X3. ....	23
Figure 11.	List of possible phases in SAM1X3. ....	24
Figure 12.	Plot of XRD peaks of possible phases in SAM1X3. ....	26
Figure 13.	Cyclic polarization measurements for SAM40 base alloy. ....	30
Figure 14.	Cyclic polarization studies of SAM1X3 as a function of heat-treatment temperature. ....	31
Figure 15.	Cyclic polarization studies of SAM1X7 as a function of heat-treatment temperature. ....	32
Figure 16.	Cyclic polarization studies of SAM3X3 as a function of heat-treatment temperature. ....	34
Figure 17.	Cyclic polarization studies of SAM3X7 as a function of heat-treatment temperature. ....	35
Figure 18.	Cyclic polarization studies of SAM4X3 as a function of heat-treatment temperature. ....	37
Figure 19.	Cyclic polarization studies of SAM4X7 as a function of heat-treatment temperature. ....	38
Figure 20.	Pourbaix Diagram for Iron (Fe). ....	49
Figure 21.	Pourbaix Diagram for Chromium (Cr). ....	50
Figure 22.	Pourbaix Diagram for Molybdenum (Mo). ....	51
Figure 23.	Pourbaix Diagram for Tungsten (W). ....	52
Figure 24.	Pourbaix Diagrams for Titanium. ....	53
Figure 25.	Pourbaix Diagram for Nickel (Ni). ....	54
Figure 26.	Overlay of SAM1X7 XRD scans as cast, heat treated to 400°C, and heat treated to 700°C. ....	55
Figure 27.	Plot of XRD peaks of possible phases in SAM1X7. ....	56
Figure 28.	List of possible phases in SAM1X7. ....	56
Figure 29.	Plot of XRD peaks of possible phases in SAM1X7. ....	57
Figure 30.	Overlay of SAM3X3 XRD scans as cast, heat treated to 400°C, and heat treated to 700°C. ....	58
Figure 31.	Plot of XRD peaks of possible phases in SAM3X3. ....	59

Figure 32.	List of possible phases in SAM3X3.....	59
Figure 33.	Plot of XRD peaks of possible phases in SAM3X3. ....	60
Figure 34.	Overlay of SAM3X7 XRD scans as cast, heat treated to 400°C, and heat treated to 700°C. ....	61
Figure 35.	Plot of XRD peaks of possible phases in SAM3X7. ....	62
Figure 36.	List of possible phases in SAM3X7.....	62
Figure 37.	Plot of XRD peaks of possible phases in SAM3X7. ....	63
Figure 38.	Overlay of SAM4X3 XRD scans as cast, heat treated to 400°C, and heat treated to 700°C. ....	64
Figure 39.	Plot of XRD peaks of possible phases in SAM4X3. ....	65
Figure 40.	List of possible phases in SAM4X3.....	65
Figure 41.	8. Plot of XRD peaks of possible phases in SAM4X3. ....	66
Figure 42.	Overlay of SAM4X7 XRD scans as cast, heat treated to 400°C, and heat treated to 700°C. ....	67
Figure 43.	Plot of XRD peaks of possible phases in SAM4X7. ....	68
Figure 44.	List of possible phases in SAM4X7.....	69
Figure 45.	Plot of XRD peaks of possible phases in SAM4X7. ....	70

## LIST OF TABLES

Table 1.	Composition of alloys analyzed.....	14
Table 2.	Thermal Properties of alloys analyzed.....	14
Table 3.	Summary of x-ray diffraction results.....	28
Table 4.	Electrochemical Parameters Measured for SAM40 Base Alloy.....	30
Table 5.	Electrochemical Measurements for SAM1X3 Alloy.....	31
Table 6.	Electrochemical Measurements for SAM1X7 Alloy.....	32
Table 7.	Electrochemical Measurements for SAM3X3 Alloy.....	33
Table 8.	Electrochemical Measurements for SAM3X7 Alloy.....	35
Table 9.	Electrochemical Measurements for SAM4X3 Alloy.....	36
Table 10.	Electrochemical Measurements for SAM4X7 Alloy.....	38
Table 11.	Summary of Electrochemical Results.....	41

THIS PAGE INTENTIONALLY LEFT BLANK

## LIST OF ACRONYMS AND ABBREVIATIONS

CP	Cyclic Polarization
CR	Corrosion Rate
CCR	Critical Cooling Rate
DARPA	Defense Advanced Research Projects Agency
EDS	Energy Dispersive X-Ray Spectroscopy
MSR	Melt-Spun Ribbon
HVOF	High-Velocity Oxy-Fuel Process:
SAM	Structural Amorphous Metal
SEM	Scanning Electron Microscopy
$E_{\text{corr}}$	Corrosion Potential
$E_{\text{pfbd}}$	Passive Film Breakdown
$E_{\text{rp}}$	Repassivation Potential
PREN	Pitting Resistance Equivalence Number
$T_g$	Glass Transition Temperature
$T_x$	Crystallization Temperature
$T_m$	Melting Temperature

THIS PAGE INTENTIONALLY LEFT BLANK



## ACKNOWLEDGMENTS

Dr. Joseph Farmer—Thanks for giving me the opportunity to work on such a fascinating project. You have been incredibly generous with your time and materials. It's been great getting to know you and work with you. You've been a great role model to Peggy and me; both professionally and nonprofessionally.

Dr. Luke Brewer—It has been a lot of fun being one of your first students. I've learned a lot from you. Your dedication as a professor has impressed and inspired. I appreciate the work you did for me on the nano-indenter.

Dr. Sarath Menon—Thank you for being extremely helpful and patient with me while I used the x-ray diffractometer and scanning electron microscope. I have learned a lot from you about material science and I always appreciate your outlook on life.

Will Young—It has been fun getting to work with you in the labs. Your knowledge far surpasses your years of experience. Without you, the labs would not be able to operate.

Lloyd Hackel—You have played a very important role in the completion of my thesis by getting my samples heat treated.

Nancy Yang—Your expertise and previous work with BMG has helped guide me through the design of my experiments and the writing of my thesis. Thank you for the time you took to meet with me and the guidance you offered. I am sorry that I was not able to work directly with you.

THIS PAGE INTENTIONALLY LEFT BLANK

# I. INTRODUCTION

## A. AMORPHOUS METALS AND BULK METALLIC GLASSES

Iron-based amorphous metals, also known as bulk metallic glasses (BMG) or structurally amorphous metals (SAMs), are alloys that have no crystalline structure and are completely vitreous. These alloys characteristically have a high strength and a high elastic modulus, which makes them potentially useful in number of applications. With the addition of carefully selected alloying constituents, BMGs can also have exceptional corrosion resistance. Compositions of several iron-based amorphous metals have been published, including those with very good corrosion resistance. The beneficial effects of chromium, molybdenum, tungsten additions on corrosion resistance of iron-based amorphous metals have been previously studied and reported.<sup>1</sup> Less is known about the possible beneficial effects of other alloying constituents on the corrosion resistance of these new materials. Even less is known about the effects of heating during processing and during service conditions on the devitrification of these alloys and the impact of such recrystallization on corrosion resistance.

Specific compositions explored in this thesis research include the amorphous iron-based metal alloy known as SAM40 ( $\text{Fe}_{52.3}\text{Mn}_2\text{Cr}_{19}\text{Mo}_{2.5}\text{W}_{1.7}\text{B}_{16}\text{C}_4\text{Si}_{2.5}$ ), which serves as the base alloy for this investigation, and compositional variations on this alloy, which include systematic variations of the nickel, yttrium, and titanium concentrations. Nickel (Ni) is added to alloys to improve both mechanical properties and corrosion resistance. In the specific case of the iron-based amorphous metals, yttrium (Y) lowers the critical cooling rate, thereby making the bulk metallic glass easier to create and more thermally stable once it is formed, thus improving the corrosion resistance.

At the outset of this research, it was hypothesized that additions of titanium could enable the formation of a protective titanium oxide film on the surface of the alloy, which is known to be extremely stable. Formation of such a protective layer on the surface of

---

<sup>1</sup> Joseph C. Farmer, "High Performance Corrosion Resistant Materials: Fe Based Amorphous Metal Coating and Composite Surfaces," Encyclopedia of Composites LLNL BOOK 462191. (2010): 4–6.

these iron-based metallic glasses could enable them to have even greater corrosion resistance than previously demonstrated. Note that titanium alloys, which are protected with titanium dioxide (rutile) films, are far more corrosion resistant in seawater than stainless steels, which are protected with chromium and molybdenum oxide layers.<sup>2</sup>

Using x-ray diffraction and corrosion analysis techniques, the effects of these alloying addition on corrosion resistance of the bulk metallic glasses as cast and reheated above their glass transition temperature have been quantified.

## **B. PROCESSING OF AMORPHOUS METALS**

Bulk metallic glasses are produced using three basic methods: melt-spinning into ribbons, drop casting ingots, and applying an atomized powder in a thermal-spray coating. The common factor between all of these methods is that they have a cooling rate that is high enough so that a glass is formed upon solidification.

Melt spinning is done by ejecting liquid metal onto a cooled, copper spinning disk, shown in Figure 1. The material solidifies on the wheel with a completely amorphous structure. Shortly after solidifying, the ribbon separates from the wheel due to thermal contraction and the centrifugal force the wheel imparts on the ribbon. The separated ribbon is thrown into a collection chamber.

Melt spinning allows for a cooling rate up to one million degrees Kelvin per second to be reached. This extremely rapid cooling allows for compositions with higher critical cooling temperatures to be formed into bulk metallic glasses. Samples prepared using this method are approximately 150 microns thick and up to several meters in length. All the samples for this thesis were prepared using this method.<sup>3</sup>

---

<sup>2</sup> Larry Kaufman, "Calculation of Coating Composites for Use in Various Corrosive Environments with Pourbaix and Thermal Stability Diagrams," (High Performance Corrosion Resistant Materials Final Report, 2004), 23.

<sup>3</sup> Joseph C. Farmer, "High Performance Corrosion Resistant Materials: Fe Based Amorphous Metal Coating and Composite Surfaces," Encyclopedia of Composites LLNL BOOK 462191 (2010): 7–8.

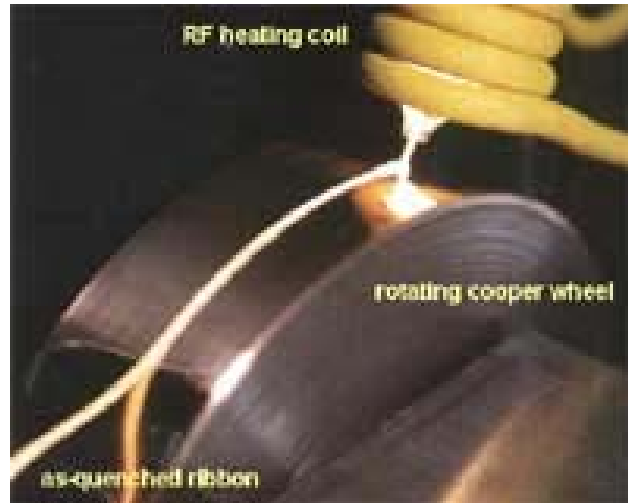


Figure 1. Melt spinning ejects molten metal onto a spinning cooled copper wheel.<sup>4</sup>

Thermal-spray uses a high-velocity oxy-fuel and is used to coat metal with the metallic glass. The process uses a combustion flame to heat and propel the atomized powder onto a base metal at speeds between mach 3 and mach 4. The deposited metal has a bond strength of 35–70 MPa and a porosity of less than 1%.<sup>5</sup> Cooling rates of ten thousand Kelvin per second can be reached. Although this process is more restrictive than melt spinning due to its lower cooling rate, it is still high enough to enable many compositions to be deposited in a vitreous state. The benefit of using thermal-spray over melt spinning is the thickness of the amorphous metal that can be achieved. Free-standing plates have been coated with a thickness of up to 20mm. This makes the metallic glasses much more useful in protecting structures from corrosion as compared to melt spun ribbons.<sup>6</sup>

---

<sup>4</sup> Nano Magnetix, “Material Science: Experimental techniques,” Nano Magnetix, [http://www.nanomagnetix.org/lectures\\_jlsanchez/index.htm](http://www.nanomagnetix.org/lectures_jlsanchez/index.htm), (accessed June 8, 2011).

<sup>5</sup> Joseph C. Farmer, et al., “Corrosion Characterization of Iron-Based High-Performance Amorphous Metal Thermal-Spray Coatings,” (paper presented at ASME PVP: Pressure Vessels and Piping Division Conference, July 17–21, 2005).

<sup>6</sup> Joseph C. Farmer, “High Performance Corrosion Resistant Materials: Fe Based Amorphous Metal Coating and Composite Surfaces,” Encyclopedia of Composites LLNL BOOK 462191 (2010): 9.

### **C. HISTORY AND BACKGROUND**

The concept of amorphous metals is fairly new. Pol Duwez invented metallic glass in the 1980s and produced a fair amount of research on solid-state amorphization and the superconductivity of metallic glasses with the collaboration of Ricardo Schwarz. In 1993, Bill Johnson, a student of Pol Duwez, discovered bulk metallic glasses, meaning that the entirety or vast majority of the metal was vitreous.<sup>7</sup>

After his discovery, Dr. Johnson founded Liquidmetal Technologies and has found applications for BMG's in places from golf club heads to a replacement for depleted uranium as a high velocity penetrator. Bill Johnson has continued his research on bulk metallic glasses including the physical principles involved in forming amorphous metals.<sup>8</sup>

Metallic glass golf clubs did not become popular for several reasons. One of the first alloys used in golf clubs was very hard and "springy", however it was also very brittle. As balls were hit with the golf club, cracks would form and spread similar to regular glass. The Liquidmetal website describes "shear bands" that form at stress concentrations in the material. In crystalline material, grain boundaries help prevent shear bands from propagating through the material. The company has found alternative alloys to reduce the brittleness. These alloys contain copper, nickel, phosphorous, and over 60% platinum. These precious metals make the golf clubs extremely expensive.<sup>9</sup>

### **D. PRACTICAL IMPLEMENTATION OF BMG**

Besides being used to make golf clubs, metallic glasses have many other potential applications. Liquidmetal predicts that they can be used for any high strength application

---

<sup>7</sup> Caltech, "Professor William L. Johnson," Caltech, <http://www.its.caltech.edu/~vitreloy/index.htm#>. (accessed June 6, 2011).

<sup>8</sup> Ibid.

<sup>9</sup> Liquidmetal Technologies, "Metallic Glass: A Drop of the Hard Stuff," <http://www.liquidmetal.com/news/dsp.news.04x105.asp>, (accessed March 15, 2011).

from tennis rackets<sup>10</sup> to scalpel blades.<sup>11</sup> The Navy has several uses for these materials that make use of their corrosion and their high elastic modulus.

## **1. Shipboard Use**

The SAM7 ( $\text{Fe}_{48}\text{Mo}_{14}\text{Cr}_{15}\text{Y}_2\text{C}_{15}\text{B}_6$ ) composition, which is also known as SAM1651 is a candidate deck plating for littoral combat ships (LCSs) and has already been used to coat the sail cover plates for submarines, as a possible approach for mitigation corrosion on the sail. Normally, ship surfaces are painted to protect them from corrosion, however flight decks are exposed to high temperatures which severely degrades, if not evaporates the paint. This limitation is especially true for ships that carry vertical takeoff, fixed wing aircraft such as the AV-8B Harrier. The deck surfaces are blasted with the exhaust of the aircraft during takeoffs and landings. A HVOF BMG coating applied to the surface of the flight deck would help protect the structure from the heat while also protecting it from corrosion of ever-present salt water.

The extreme hardness and corrosion resistance of BMGs also makes them ideal for use on the bows of icebreakers. These properties are also highly ideal for shafts in systems that require corrosion resistance, low flex, and a hard surface. In this case, the BMG would again likely be applied to the surface with a HVOF spray coating.<sup>12</sup>

## **2. Spent Nuclear Fuel Storage**

Current container designs for the geologic disposal of spent nuclear fuel and high-level radioactive wastes specify the use of nickel-based alloy C-22 as a corrosion resistant outer layer. This particular application is especially demanding since these packages will reach surface temperatures of 180°C, will experience substantial gamma ray irradiation of the surrounding environment, leading to the formation of radiolysis

---

<sup>10</sup> Liquidmetal Technologies, “Liquidmetal Sporting Goods and Leisure Products,” <http://www.liquidmetal.com/applications/dsp.sporting.asp>, (accessed June 6, 2011).

<sup>11</sup> Liquidmetal Technologies, “Liquidmetal Medical Devices,” <http://www.liquidmetal.com/applications/dsp.medical.asp>, (accessed June 6, 2011).

<sup>12</sup> Joseph C. Famer, “High Performance Corrosion Resistant Material Project’s New Iron-Based Amorphous Metal Coatings: Enhanced Corrosion Performance and Substantial Cost Savings,” (presentation at Nuclear Waste Technical Review Board, Washington DC, November 16, 2005).

products, such as hydrogen peroxide, and must maintain their integrity in the presence of hot, evaporatively concentrated, geothermal brines. Unfortunately, these nickel based alloys are quite expensive, with documented costs of at least \$37 per pound. The iron-based amorphous metals proposed here promise to provide comparable corrosion resistance, but at a substantially lower cost, believed to be on the order of \$7 per pound when deposited in the form of an HVOF coating. Given the life cycle cost of such repositories, with cost estimates ranging from \$58 billion in 2002 to more recent estimates approaching \$130 billion, this cost differential for constructing the 11,000 required containers could save the nation several tens-of-billions of dollars.<sup>13</sup>

These materials also promise to be exceptional criticality control materials for applications on the basket assembly used to support the spent fuel rods inside the containers. The best known borated materials have absorption cross-sections for thermal neutrons of less than  $2\text{cm}^{-1}$ , whereas the materials being investigated here have substantially higher boron concentrations, with the boron homogeneously dispersed throughout the material, and have absorption cross-sections for neutrons of more than  $7\text{cm}^{-1}$ , the highest known value for any known material proposed for this application. Such materials are therefore important for the future of fission energy.<sup>14</sup>

---

<sup>13</sup> Joseph C. Famer, “High Performance Corrosion Resistant Material Project’s New Iron-Based Amorphous Metal Coatings: Enhanced Corrosion Performance and Substantial Cost Savings,” (presentation at Nuclear Waste Technical Review Board, Washington DC, November 16, 2005).

<sup>14</sup> Ibid.



## **II. EXPERIMENTAL HYPOTHESES**

This thesis research measures the effects of three carefully selected alloying additions, nickel, yttrium, and titanium, to base alloy SAM40 on devitrification and corrosion resistance. Each alloying addition was chosen for a specific reason and has its own expected result. The following section discusses the reasons that each alloying addition was selected and how they will influence the materials devitrification and corrosion resistance.

### **A. NICKEL ADDITION**

Nickel is present in many highly corrosion resistant alloys. In addition to the chromium, molybdenum, and manganese that have already been added to make SAM40 base alloy, nickel is expected to further improve the corrosion resistance and improve the mechanical properties.

### **B. YTTRIUM ADDITION**

Yttrium was added to SAM40 base alloy to lower the critical cooling rate to establish a bulk metallic glass. This addition will hopefully make it easier to manufacture and install bulk metallic glass with better results. HVOF spray coatings are a very effective way to deposit metallic glass on the surface of a structure; however, the cooling rates are not always as high as other methods of creating BMG such as melt-spinning. The yttrium addition will potentially improve the quality of HVOF sprayed BMG. Higher quality BMG has less crystallinity will have better corrosion resistance because it will have a more homogenous microstructure and less nucleation sites for corrosion to attack.

It is further hypothesized that additions of yttrium could enable the formation of a protective yttrium oxide film ( $Y_2O_3$ ) on the surface of the alloy, a passive film known to be extremely stable. Formation of such a protective layer on the surface of these iron-based metallic glasses could enable them to have even greater corrosion resistance than

previously demonstrated. <sup>15</sup>Note that titanium alloys, which are protected with titanium dioxide (rutile) films, are far more corrosion resistant in seawater than stainless steels, which are protected with chromium and molybdenum oxide layers.

### **C. TITANIUM ADDITION**

It is hypothesized that additions of titanium could enable the formation of a protective titanium oxide film (TiO<sub>2</sub>) on the surface of the alloy, a passive film known to be extremely stable. Formation of such a protective layer on the surface of these iron-based metallic glasses could enable them to have even greater corrosion resistance than previously demonstrated. Note that titanium alloys, which are protected with titanium dioxide (rutile) films, are far more corrosion resistant in seawater than stainless steels, which are protected with chromium and molybdenum oxide layers.<sup>16</sup>

---

<sup>15</sup> Jian Xu, et al., “Studies on the Corrosion Behavior of Yttrium-Implanted Zircaloy-4,” *Journal of Materials Science* 35 (2000) 6225–6229.

<sup>16</sup> Larry Kaufman, “Calculation of Coating Composites for Use in Various Corrosive Environments with Pourbaix and Thermal Stability Diagrams,” (High Performance Corrosion Resistant Materials Final Report, 2004), 23.

### III. COMPOSITIONAL CORROSION CHARACTERISTICS

#### A. EMPIRICAL METHODS USED IN DESIGNING ALLOYS FOR CORROSION RESISTANCE

##### 1. Pitting Resistance Equivalence Number

One of the first and most basic estimates for an austenitic alloy's corrosion resistance is its pitting resistance equivalence number. (PREN) PREN is an empirical way for comparing the corrosion resistance of stainless steels. This type of empirical correlation has also been used to estimate the corrosion resistance of nickel-based alloys. PREN is calculated using one of two equations:

$$PREN = [\%Cr] + 3.3 \times [\%Mo + \%W] + 30 \times [\%N] \quad (1)$$

$$PREN = [\%Cr] + 3.3 \times ([\%Mo] + 0.5 \times [\%W]) + k \times [\%N] \quad (2)$$

The second equation was developed because it was recognized that some alloys that performed better in testing had a lower PREN than alloys that performed worse. The factor k is a coefficient that adjusts the importance of the effects of nitrogen. It can range from 12.8 to 30, however 16 is generally accepted.<sup>17</sup>

These equations have been used to estimate the corrosion resistance of previous BMG formulations including SAM40 and its predecessors. If the PREN estimate approach is applied to the alloys analyzed in this paper, the equation must be modified to account for the additions of Ni, Y, and Ti. It would be reasonable to describe the BMG PREN as the PREN of SAM40 plus linear contributions for each of the new additives as shown in Equation 3.

$$PREN_{BMG} = PREN_{SAM40} + A \cdot [\%Ni] + B \cdot [\%Y] + C \cdot [\%Ti] \quad (3)$$

With the knowledge gained in this research thesis, it will be possible to estimate the relative weighting coefficients, A, B, and C, which will enable PREN to be applied to a larger variety of bulk metallic glasses.

---

<sup>17</sup> Joseph C. Farmer, "High Performance Corrosion Resistant Materials: Fe Based Amorphous Metal Coating and Composite Surfaces," Encyclopedia of Composites LLNL BOOK 462191 (2010): 5.

## 2. Pourbaix Diagrams

Another method for predicting the corrosion resistance of new iron-based alloys is the use of Pourbaix diagrams. Pourbaix diagrams account for both the complexity of the alloy and the range of constituents in the service environment, e.g., seawater. Pourbaix diagrams are created by solving the Nernst equation at various potentials and pH's. The constituent diagrams can be overlaid and an overall Pourbaix Diagram can be created. The overlays help to identify weak spots where at certain potentials and pH's the alloy will be susceptible to corrosion. As the spots are identified, the composition can be adjusted and elements can be added which have strong passive regions where active corrosion exist.

This was done repeatedly for various compositions of bulk metallic glasses in order to maximize the corrosion resistance. This approach was one the major guiding principles in the evolution of the BMGs. Figure 2 shows the composite Pourbaix diagram for all the constituents of iron-based alloy SAM40. The regions inside the band of passive oxide films offers more protection to the material from active corrosion. The areas outside the band are where passive films break down and active corrosion occurs more easily. By adding constituent alloys that extend the area of the band, the material will be more corrosion resistant in more conditions.<sup>18</sup>

Unfortunately, nickel (Pourbaix diagram shown in Figure 25) does not have a definitive oxide film that extends beyond the area of the proactive oxide film region. Even though nickel's passive film region does not extend beyond the current region, it could still improve the corrosion resistance by bolstering the strength and redundancy of the existing passive film region.

The red line on Figure 2 shows the theoretical benefit of adding titanium to SAM40. The extremely stable passive film, titanium oxide, increases the area protected from active corrosion substantially. More Pourbaix diagrams for the constituent elements are included in the appendix. Pourbaix diagrams for yttrium were not available, however

---

<sup>18</sup> Larry Kaufman, "Calculation of Coating Composites for Use in Various Corrosive Environments with Pourbaix and Thermal Stability Diagrams," (High Performance Corrosion Resistant Materials Final Report, 2004), 2–17.

the effect on the passive film region would be similar to titanium. Note that the passive film is a secondary effect of adding yttrium. The primary purpose for adding yttrium is to improve the stability of the amorphous microstructure and making the BMG easier to manufacture.

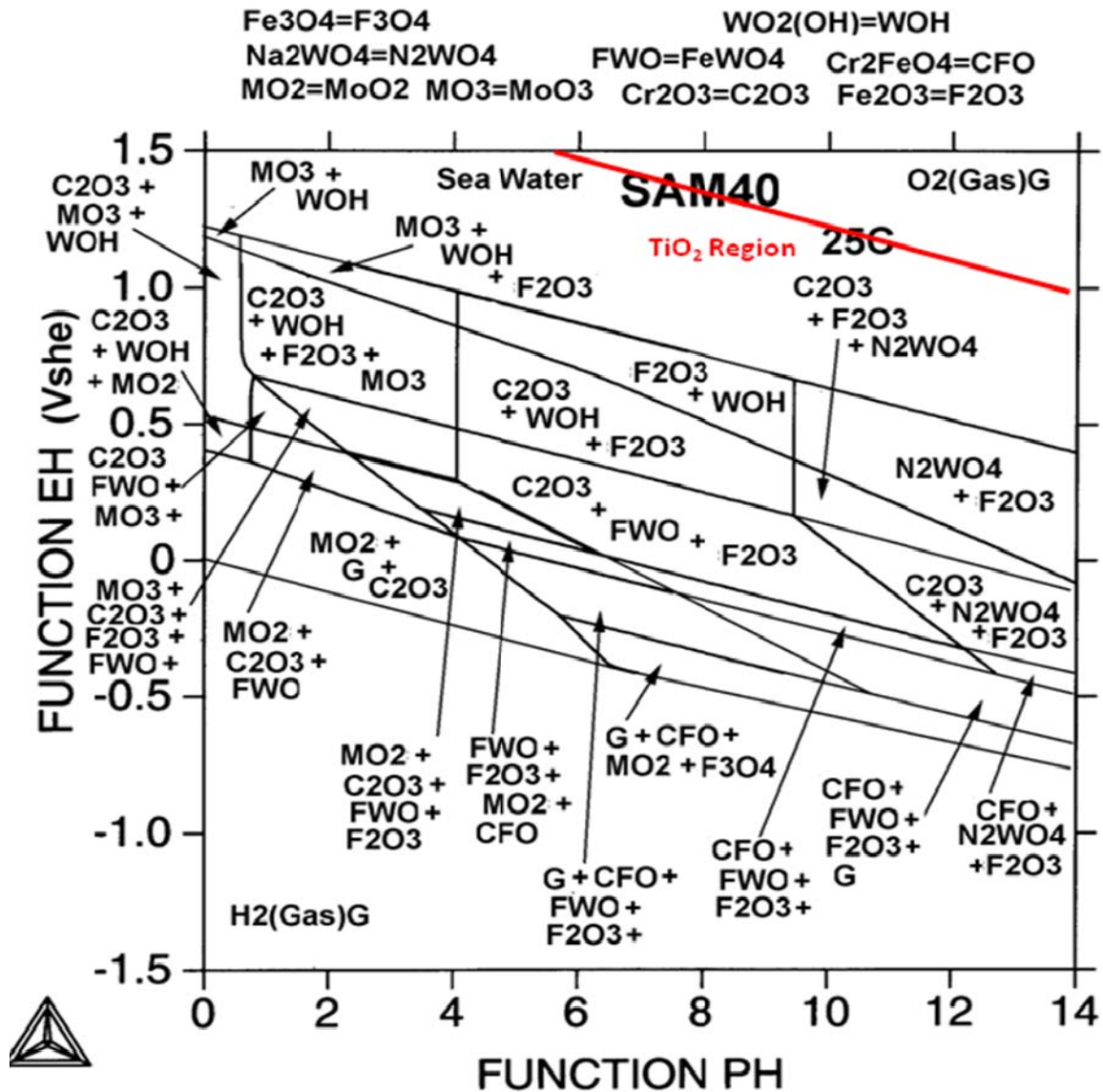


Figure 2. Overlaid Pourbaix Diagram of SAM40.<sup>19</sup>

<sup>19</sup> Larry Kaufman, "Calculation of Coating Composites for Use in Various Corrosive Environments with Pourbaix and Thermal Stability Diagrams," (High Performance Corrosion Resistant Materials Final Report, 2004), 3.

THIS PAGE INTENTIONALLY LEFT BLANK

## IV. EXPERIMENTAL DESIGN

### A. COMPOSITION OF SAM40 BASE ALLOY AND ITS DERIVATIVES

Using the melt-spinning process and its high cooling rate, many compositions were successfully produced as bulk metallic glasses. These compositions were created in order to find better performing alloys in the area of corrosion resistance. One set of compositional modifications started with SAM40 ( $\text{Fe}_{52.3}\text{Mn}_2\text{Cr}_{19}\text{Mo}_{2.5}\text{W}_{1.7}\text{B}_{16}\text{C}_4\text{Si}_{2.5}$ ) as a base alloy and added specific elements at intervals of 1, 3, 5, and 7 atomic percent. The elements added were nickel, molybdenum, yttrium, titanium, and zirconium. The alloys were named structurally amorphous metals with a two number identifier. The first number designates the alloying element and the second describes the amount of the addition in atomic percentage. For example, SAM1X1 has a one atomic percent nickel addition. SAM4X7 has a seven atomic percent addition of titanium.

These compositions were verified using energy dispersive x-ray spectroscopy (EDS) on a Quanta Series 200 environmental SEM. There was a notable difference in the roughness of the side of the ribbon that had been in contact with the cooled copper wheel. The rough side also had small traces of copper present that had been transferred to the melt spun ribbon during the cooling process. Each composition was analyzed at three random locations and scanned at a magnification of 10,000X. The averages are reported in Table 1.<sup>20</sup> Theoretical thermodynamic properties were calculated for each composition and are reported in Table 2. The expected crystallization temperatures for this new family of alloys should lie between 540–700°C.

---

<sup>20</sup> Joseph C. Farmer, et al., “Corrosion Characterization of Iron–Based High–Performance Amorphous Metal Thermal–Spray Coatings,” (paper presented at ASME PVP: Pressure Vessels and Piping Division Conference, July 17–21, 2005).

Table 1. Composition of alloys analyzed.<sup>21</sup>

Alloy	Specification / Formula	Fe	Cr	Mn	Mo	W	B*	C*	Si	Y	Ni	Ti	Total
SAM40	Fe <sub>52.3</sub> Mn <sub>2</sub> Cr <sub>19</sub> Mo <sub>2.5</sub> W <sub>1.7</sub> B <sub>16</sub> C <sub>4</sub> Si <sub>2.5</sub>	52.3	19.0	2.0	2.5	1.7	16.0	4.0	2.5	0.0	0.0	0.0	100
SAM1X3	(SAM40) <sub>97</sub> + Ni <sub>3</sub>	50.7	18.4	1.9	5.4	1.6	15.5	3.9	2.4	0.0	3.0	0.0	100
SAM1X7	(SAM40) <sub>93</sub> + Ni <sub>7</sub>	48.6	17.7	1.9	9.3	1.6	14.9	3.7	2.3	0.0	7.0	0.0	100
SAM3X3	(SAM40) <sub>97</sub> + Y <sub>3</sub>	50.7	18.4	1.9	2.4	1.6	15.5	3.9	2.4	3.0	0.0	0.0	100
SAM3X7	(SAM40) <sub>93</sub> + Y <sub>7</sub>	48.6	17.7	1.9	2.3	1.6	14.9	3.7	2.3	7.0	0.0	0.0	100
SAM4X3	(SAM40) <sub>93</sub> + Ti <sub>7</sub>	50.7	18.4	1.9	2.4	1.6	15.5	3.9	2.4	0.0	0.0	3.0	100
SAM4X7	(SAM40) <sub>93</sub> + Ti <sub>7</sub>	48.6	17.7	1.9	2.3	1.6	14.9	3.7	2.3	0.0	0.0	7.0	100

Table 2. Thermal Properties of alloys analyzed.<sup>22</sup>

Alloy	Tg (°C)	Tx (°C)	Tm (°C)
SAM40	568-574	623	1110
SAM1x3	560	589	1119
SAM1x7	510	545	1112
SAM3x3	573	659	1138
SAM3x7	not clear	697	1164
SAM4x3	568	623	1146
SAM4x7	558	616	1198

## B. ALLOY AND HEAT TREATMENT TEMPERATURE SELECTION

Nickel, yttrium, and titanium additions to SAM40 base alloy have been chosen for analysis of their effect on corrosion resistance and how they affect the stability of the amorphous microstructure. SAM40 was used as a control for comparison. In addition to comparing the effects on as cast samples, the samples were heat treated to analyze the effects of the alloy addition at temperatures near and above the glass transition temperature and crystallization temperature. The heat treatment temperatures chosen for analysis are as cast, 400°C, and 700°C. The amount of alloying element added to the base alloy that was chosen for analysis was three and seven atomic percent. This

<sup>21</sup> Joseph C. Farmer et al., “High Performance Corrosion Resistant Iron Based Amorphous Metal Coatings: Evaluation of Corrosion Resistance,” (High Performance Corrosion Resistant Materials Annual Report, 2005), 26.

<sup>22</sup> Ibid., 27.



compositional range is large enough to expect a distinguishable difference in the results. This addition diluted the SAM40 composition to 97% and 93%, respectively, as shown in the Table 1.

## **C. HEAT TREATMENT**

### **1. Argon Purged Furnace**

A small furnace was set up in the materials lab at the Naval Postgraduate School to allow samples to be prepared on site. (Figure 3) The samples were placed in a small Pyrex tube that was open at both ends. Glass fiber was put in the bottom of the tube to prevent the melt-spun ribbon samples from falling out. The Pyrex tube was placed in a copper test tube with a small bleed hole. The tube was connected to a vacuum pump and to the argon tank through a three-way valve.



Figure 3. Photograph showing the copper test tube connected to the vacuum/argon tubing inside the furnace.

First, a vacuum (shown in Figure 4) would be drawn on the sample with the bleed hole plugged. The three way valve would then be positioned to send argon gas into the sample. As pressure built in the copper tube, the plug would be removed allowing the gas to slowly flow and flush out any residual oxygen. The furnace was then turned on and heated until reaching the desired temperature where it would be held for one hour. Argon was supplied continuously throughout the test.



Figure 4. Photograph of the assembled argon purged furnace. The vacuum pump is seen below the counter.

## 2. Sandia Argon Purged Furnace

A set of melt-spun ribbon samples were sent to Sandia National Laboratory in Livermore, CA to be annealed in an industrial argon furnace. The samples had a vacuum

drawn on them before applying a supply of argon gas to them. The samples were heat treated for one hour and cooled under continuous argon flow to room temperature.

### **3. Vacuum Furnace**

A set of melt-spun ribbon samples were sent to Metal Improvements Company to be heat treated. The samples were separated and labeled by composition. When received by Metal Improvements Company, they put a piece of ribbon of each alloy composition in a tantalum foil wrap. One piece of ribbon was laid in each fold and the foil was etched with the composition. When all the ribbons were enclosed in the wrap, the ends were folded up to prevent the ribbons from sliding out.

Five tantalum foil packets were heat treated to five different temperatures: 300, 400, 500, 600, and 700 degrees Celsius. Each foil packet was heated up to its designated temperature and held there for one hour. The furnaces were then allowed to cool. A vacuum was drawn on the furnace throughout the heat treatment and cooling to prevent oxidation of the samples. Tantalum also scavenges oxygen which further protects the bulk metallic glass melt spun ribbons from oxidizing.

### **D. X-RAY DIFFRACTION SETUP AND PROCEDURE**

X-ray diffraction testing was performed on the samples, heat treated using Metal Improvements Company's vacuum furnace, to measure varying degrees of devitrification. The machine used was a Philips XRD model PW1830, shown in Figure 5. It uses copper x-rays generated by a 35KeV 30mA electron beam. The samples were scanned continuously at a rate of .01 degrees per second with an angle ranging from 20 to 90 degrees. The tests took approximately two hours.



Figure 5. Photograph of x-ray diffractometer.

Ribbons were scanned that had not been processed in any way other than the heat treatment. Pieces of ribbon approximately one inch in length were placed on a glass slide, aligned in the direction of the x-ray beam. A small dab of vacuum grease was used to hold the samples in place at either end during the scan. (Figure 6)

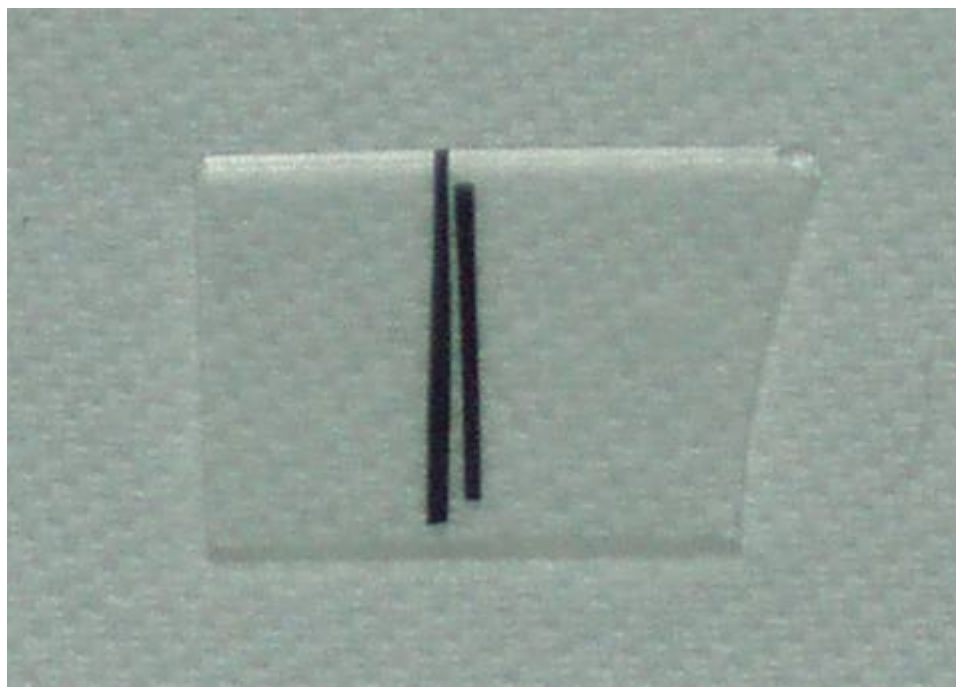


Figure 6. Photograph of melt-spun ribbons mounted on glass slide for an XRD scan.

#### **E. CYCLIC POLARIZATION SETUP AND PROCEDURE**

Cyclic polarization testing increases the corrosion potential of a sample at a constant rate up to a set point, then reverses and decreases the corrosion potential until it ends at the sample material's corrosion potential. For this test the samples were mounted on a titanium disk using scotch tape so that a conductive path was created and only the sample material was exposed to the electrolyte.

The test apparatus uses a sealed cell, filled with salt water and sitting in a heater (Figure 7). Nitrogen was bubbled through the electrolytic solution to remove oxygen. A condenser and a gas trap were used to prevent moisture from leaving the cell and changing the electrolyte concentration. A Ag/AgCl reference electrode was used to measure the cell potential and a graphite rod was used for the counter and counter sense. The working and working sense wires were connected to the sample mount. The system was grounded through the ring stand and lab bench.



Figure 7. Photograph of the cyclic polarization test apparatus.

The potential was controlled with respect to the material's corrosion potential ( $E_{\text{corr}}$ ). The test was started with a potential of one volt below corrosion potential making the reaction cathodic. Potential was increased at a rate of 5 mV/s, until it reached the apex at 1.5 volts above the  $E_{\text{corr}}$ . At this point the potential reverses and decreases at the same rate until it ends at the  $E_{\text{corr}}$ . All tests were run at 30°C.



## V. EXPERIMENTAL RESULTS

### A. STRUCTURAL CHARACTERIZATION OF MELT-SPUN RIBBONS

#### 1. SAM40 Base Alloy

The SAM40 base alloy has been analyzed thoroughly in the past. Figure 8 shows XRD scans of SAM40 heated to various temperatures above and below the glass transition temperature. These scans were not done on melt-spun ribbons, which is why they have much lower background than the samples analyzed for this paper. Based on the peaks present in the 800°C and 1000°C samples, it was suspected that phases present were ferrite (body centered cubic),  $M_{23}C_6$ , and  $Cr_2B$ .

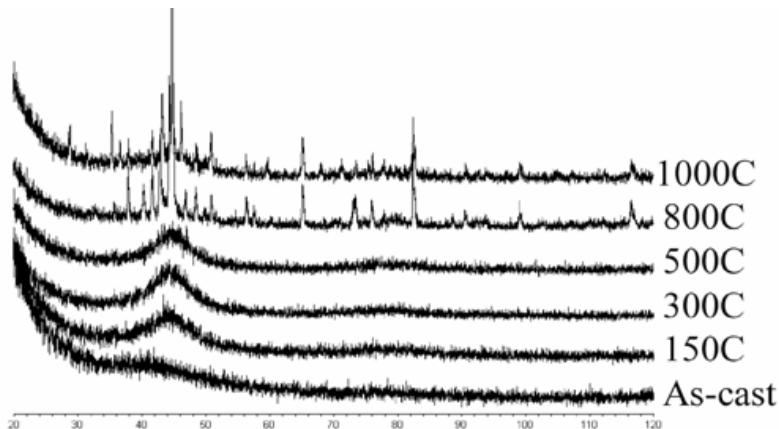


Figure 8. SAM 40 XRD scan at multiple temperatures.<sup>23</sup>

#### 2. SAM1X3 and SAM1X7 (Nickel Addition)

In the as cast sample (blue), a broad peak centered was observed around 44 degrees, as seen previously in structurally amorphous metals. Previous analyses did not show the broad peak centered around 25 degrees. This was determined to be background cause by the glass slides. It is present in varying degrees because of the variation in melt-spun ribbon size. The better the x-ray beam was aligned with the sample and the larger the sample was, the less background that was present. The broad peaks are expected

---

<sup>23</sup> Nancy Yang et al., “Devitrification and Its influence on Corrosion Performance of SAM2x5 and SAM1651” (High Performance Corrosion Resistant Materials Annual Report, 2005), 11.

because neither the silica glass slide nor the amorphous metal sample has a crystalline structure. The same is seen in the 400°C sample. It has not been heated above the glass transition temperature and no crystalline phases have precipitated out. The plots for each sample have been stacked vertically to prevent overlapping. The heat-treating temperature does not cause the entire sample to have a higher intensity count.

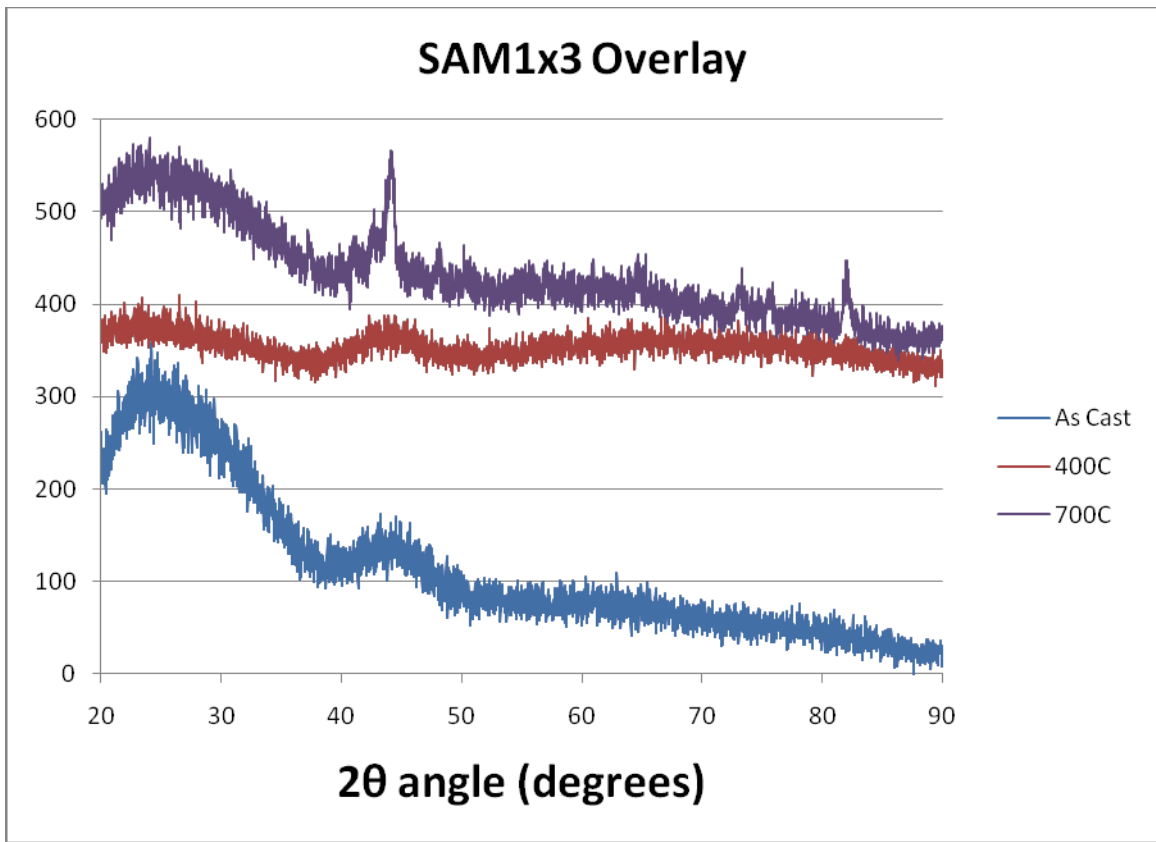


Figure 9. Overlay of SAM1X3 XRD scans as cast, heat treated to 400°C, and heat treated to 700°C.

The sample heated to 700°C displayed sharp peaks, which indicate the presence of crystalline phases. In Figures 10–12, the 700°C was analyzed using X’Pert Highscore which compares known diffraction patterns contained in a crystallographic database to the peaks present in order to determine what phases are present. The elements present in the sample are input into the program, but it does not know how much of each element is present.



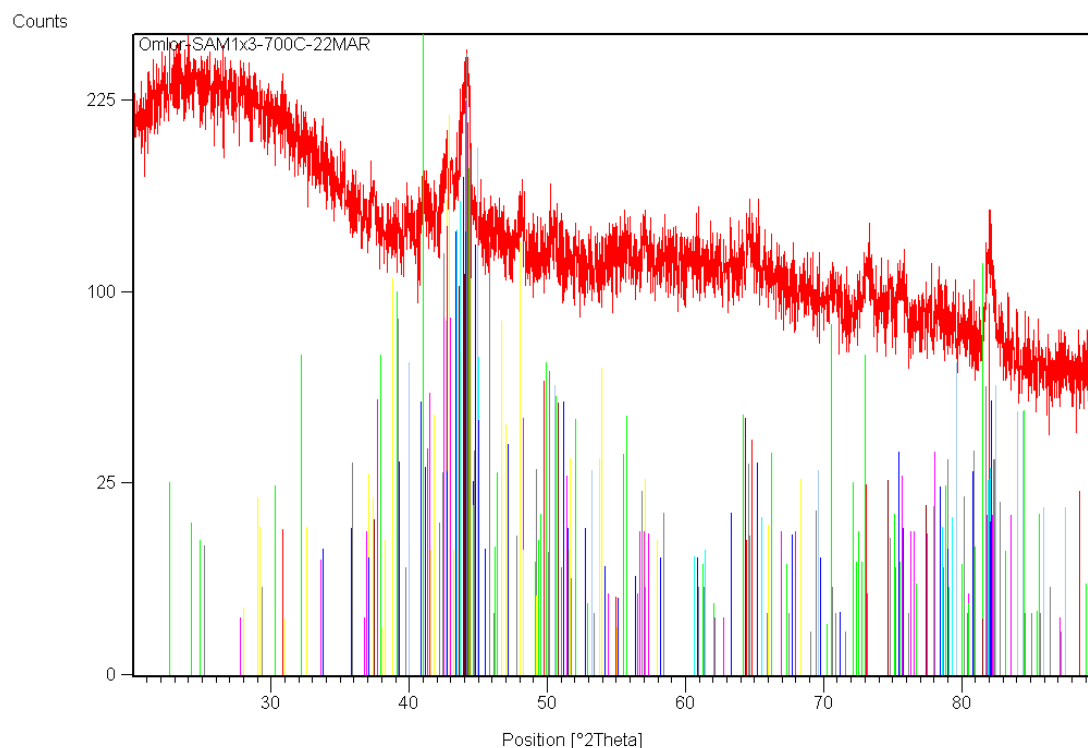


Figure 10. Plot of XRD peaks of possible phases in SAM1X3.

The program outputs a list of phases that could be present in the sample based on their x-ray diffraction peaks, and how those compare to the peaks present in the scan. The user must select what phases are likely to be present and which are not. Those that were selected are shown in Figure 11. For example, the program sees that carbon is present in the sample and thinks that graphite and other forms of elemental carbon, including fullerene and diamonds, are present. This is unlikely because of the low carbon composition of the samples and the homogeneity of the molten metal used in the melt spinning process.

No.	Visi...	Ref. Code	Compoun...	Chemical For...	Sc...	Scal...	Sem...
1	✓	00-054-0...	Manganes...	Mn Ni	32	0.743	-
2	✓	00-012-0...	Awaruite	(Ni, Fe)	31	0.605	-
3	✓	00-001-1...	Chromium	Cr	21	0.826	-
4	✓	00-006-0...	Chromium...	Cr	20	0.676	-
5	✓	00-049-1...	Silicon Car...	Si C	20	0.392	-
6	✓	00-044-1...	martensite	C0.12 Fe1.88	13	0.547	-
7	✓	00-035-0...	Chromium ...	Cr23 C6	12	0.805	-
8	✓	00-037-0...	Iron Carbide	Fe2 C	9	0.551	-
9	✓	00-034-0...	434-L stain...	Fe - Cr	9	0.673	-
10	✓	00-044-1...	martensite	C0.055 Fe1.945	20	0.919	-
11	✓	00-038-1...	Boron Chr...	Cr2 B	8	0.627	-
12	✓	00-036-1...	heptachro...	Cr7 C3	15	0.940	-
13	✓	00-047-1...	Iron Nickel	Fe0.64 Ni0.36	7	0.368	-
14	✓	00-044-1...	martensite	C0.14 Fe1.86	6	0.484	-
15	✓	00-017-0...	Iron Carbide	Fe2 C	3	0.312	-
16	✓	00-039-1...	Boron Iron	Fe3 B	3	0.764	-
17	✓	00-052-0...	α-Fe, aust...	Fe	6	0.491	-
18	✓	00-051-0...	γ-Fe5 C2, ...	Fe5 C2	6	0.480	-
19	✓	00-025-0...	Boron Mol...	Mo2 B	2	1.046	-
20	✓	00-025-0...	Boron Nic...	Ni2 B	0	0.456	-
21	✓	00-014-0...	Nickel Car...	Ni C	-	-	-
22	✓	00-048-1...	Boron Nic...	B Ni2	-	-	-

Figure 11. List of possible phases in SAM1X3.

When the peaks of the possible phases (multi-colored) are plotted against the scan plot (red on Figure 10), we can see that large groups of peaks are seen where there are peaks on the scan. The program adjusts the scaling of the peaks to what it thinks the composition of each should be, but because the composition of the sample is very complex, the program cannot accurately predict the quantity of each phase that is present. Also, many phases have similar peaks such as those containing iron, chromium, and nickel. This is well illustrated in Figure 12, which shows that many of the phases that are likely present have peaks around 44 degrees. Because of this, we cannot assume that the peaks are caused by any single phase. They are more likely caused by the presence of many phases in smaller quantities. The base alloy, SAM40 (Fe52.3Mn2Cr19Mo2.5W1.7B16C4Si2.5), has eight components with one component added, Ni, Y, or Ti, for a total of nine. By the Gibbs phase rule, the maximum number of phases possible in equilibrium is

$$F = C - P + 2 \quad (4)$$

where  $F$  is the number of degrees of freedom,  $C$  is the number of chemical components in the system, and  $P$  is the number of phases in equilibrium. For the alloys in this thesis, the maximum number of phases that can co-exist in equilibrium is eleven. It would be more reasonable to assume that the maximum should be no more than nine for most regions of phase equilibria. It should be noted that BMGs almost by definition are not in equilibrium, but the Gibbs phase rule gives an upper estimate on the number of expected phases. The high score software does not have this knowledge; it simply suggests phases based on “best fit” between the diffraction pattern and the database. With the low signal levels in these measurements, we cannot identify individual crystalline phases; however, we can state whether crystalline phases are present and whether they might be the same from one alloy to the next.<sup>24</sup>

---

<sup>24</sup> Computational Thermodynamics, “Gibbs Phase Rule,” CALPHAD, [http://www.calphad.com/gibbs\\_phase\\_rule.html](http://www.calphad.com/gibbs_phase_rule.html) (accessed June 12, 2011).

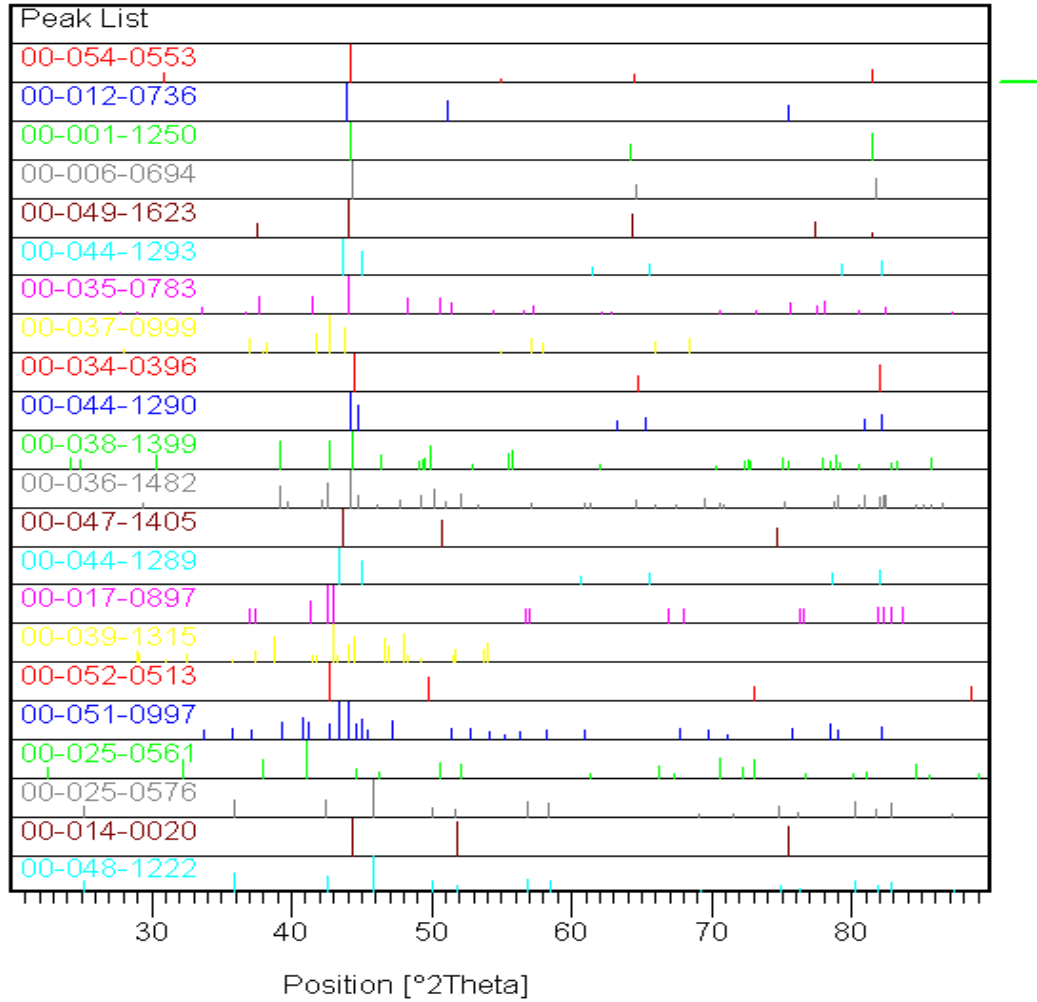


Figure 12. Plot of XRD peaks of possible phases in SAM1X3.

SAM1X7 contains seven atomic percent of nickel added to base alloy SAM40. The as cast sample (blue) and the sample heat treated at 400°C (red) appear to be fully amorphous. There is a variation in the background caused by the glass slide. This is most likely due to variations in sample size and slight misalignments in the mounting. The sample heat treated to 700°C (violet) shows sharp peaks indicating that there are crystalline phases present.

The peaks in the SAM1X7 700°C sample seem to be less intense than those in the 1X3 700°C sample. The peaks around 82 degrees do not appear at all. This demonstrates that there are different phases present, which is likely an effect of the extra nickel. Based on the lists of possible phases and their diffraction patterns, there appears to be less chromium and iron phases present in the SAM 1X7 sample. It is difficult to quantify the difference because of the complex composition of the alloys.

### **3. SAM3X3 and SAM3X7 (Yttrium Addition)**

SAM3X3 has three atomic percent of yttrium added to base alloy SAM40. We can see that the as cast (blue) and 400°C (red) samples are amorphous once again and the 700°C (violet) sample shows some evidence of crystalline phases. The peaks present are even less intense than those seen in SAM1X3 and SAM1X7 with the nickel addition.

The crystalline constituent still appear to be composed mostly iron and chromium, but in much lower quantity. The secondary peaks chromium and iron peaks shown in Figure 30 at 81° and 82° are barely visible above the background. The only phase containing yttrium is YSi<sub>2</sub>, but there is very little, if any, present.

SAM3X7 is very similar to SAM 3X3 in that the peaks are less intense than the nickel containing samples. SAM3X7 does have a slightly higher peak around 44° than SAM3X3, but not by much. Iron and chromium continue to make up most of the crystalline phases, however none of the potential phases scored very high. Yttrium seems to have improved the materials ability to approve devitrification, which is demonstrated by SAM3X3 and 3X7. This has the potential to improve the corrosion resistance.

### **4. SAM4X3 and SAM4X7 (Titanium Addition)**

SAM4X3 has a three atomic percent titanium addition to base alloy SAM40. The as cast (blue) and 400°C (red) samples have smooth, broad peaks centered at 44 degrees showing that they are amorphous. High intensity peaks appeared in the 700°C sample (violet). These are the highest intensity peaks seen in the testing with intensities at over 300 counts above the background. Likewise, we also see the highest scores for phases that are likely present. Iron and chromium phases appear the most prevalent, which is

expected since they dominate the composition at 50.7% and 18.4%, respectively. Titanium shows up in mixtures with iron and chromium, but not in the expected carbides or borides. Although these phases are potentially present, they do not exist in any large quantity.

SAM4X7 has similar x-ray diffraction results to SAM4X3, but with slightly lower intensity. Either titanium was increased high enough that it helped to reduce devitrification, or, more likely, the lower intensity is a result of the varying sample size. The compositions are similar with a slightly higher relative score for titanium mixed with iron and chromium. Once again, titanium carbide and titanium boride did not appear in any large quantity. Because both the 700°C samples containing titanium had large peaks we can conclude that titanium does not improve devitrification.

## 5. Summary of X-ray Diffraction Results

The x-ray diffraction confirmed that all melt-spun ribbon samples were amorphous as cast and when heat treated to 400°C. Samples with yttrium had the lowest intensity peaks and the samples with titanium had the highest intensity peaks. Although we cannot identify what phases are present from the relative weak peaks, we can see that the alloy addition does affect whether crystalline phases are present and if they differ between composition. This is shown by the difference in the peaks that are visible, shown in Table 3.

Table 3. Summary of x-ray diffraction results.

Alloy	As Cast	Heat Treated to 400°C	Heated Treated to 700°C	Counts above background	2 $\theta$ Location of peaks
SAM1X3	Amorphous	Amorphous	Devitrified	120	44, 65, 73, 76, 82
SAM1X7	Amorphous	Amorphous	Devitrified	100	43, 46, 49, 75
SAM3X3	Amorphous	Amorphous	Devitrified	80	44, 83
SAM3X7	Amorphous	Amorphous	Devitrified	80	44
SAM4X3	Amorphous	Amorphous	Devitrified	300	43, 44, 65, 82
SAM4X7	Amorphous	Amorphous	Devitrified	220	43, 44, 65, 79, 82

## **B. ELECTROCHEMICAL CORROSION ANALYSIS OF MELT SPUN RIBBONS**

### **1. Studies of SAM40 Base Alloy**

As potential increased from approximately -1100 mV, current decreased until the corrosion potential was reached at -251 mV. As potential was increased in the as cast sample (blue), we saw that current increased around a potential of zero mV. This was likely due to the oxidation of molybdenum. As the reaction stabilized, current returned to its previous trend. As the potential approached the test limit of approximately 1300mV, the passive film began to break down and current increased. Before the passive film could fully break down, potential started to reverse and the plot retraced itself. There was no repassivation potential because of the retracing. (Figure 13)

In the sample heat treated at 600°C (red), we saw a similar corrosion potential of -258 mV. The reaction that we attributed to molybdenum was seen again, although it had a smaller effect on current. As the maximum potential reached in the test, current peaked as the passive film broke down similarly to the as cast sample, but did not retrace the plot as potential reversed. A repassivation potential could be seen, although it was difficult to state the value because of the molybdenum phenomenon. The general corrosion resistance of this sample decreased as compared to the as cast sample.

In the sample heat treated to 800°C (violet), we saw very little resistance to corrosion. The corrosion potential has decreased to -526 mV, meaning that the anodic reaction would occur sooner. When this happened, current increased and the sample corroded actively.

The general trend that was expected as these metallic glasses were heated is that they would become less corrosion resistant. This is because when they were heated to temperatures near or above their glass transition temperature, (approximately 500°C) they will begin to devitrify. Crystalline phases, which were not as resistant to corrosion, would begin to appear in the glassy matrix.

Table 4. Electrochemical Parameters Measured for SAM40 Base Alloy.

	$E_{\text{corr}}$ (mV)	$E_{\text{pfbd}}$ (mV)	$E_{\text{rp}}$ (mV)
SAM40 as cast	-251	1282	NA
SAM40-600°C	-258	626	NA
SAM40-800°C	-526	-361	NA

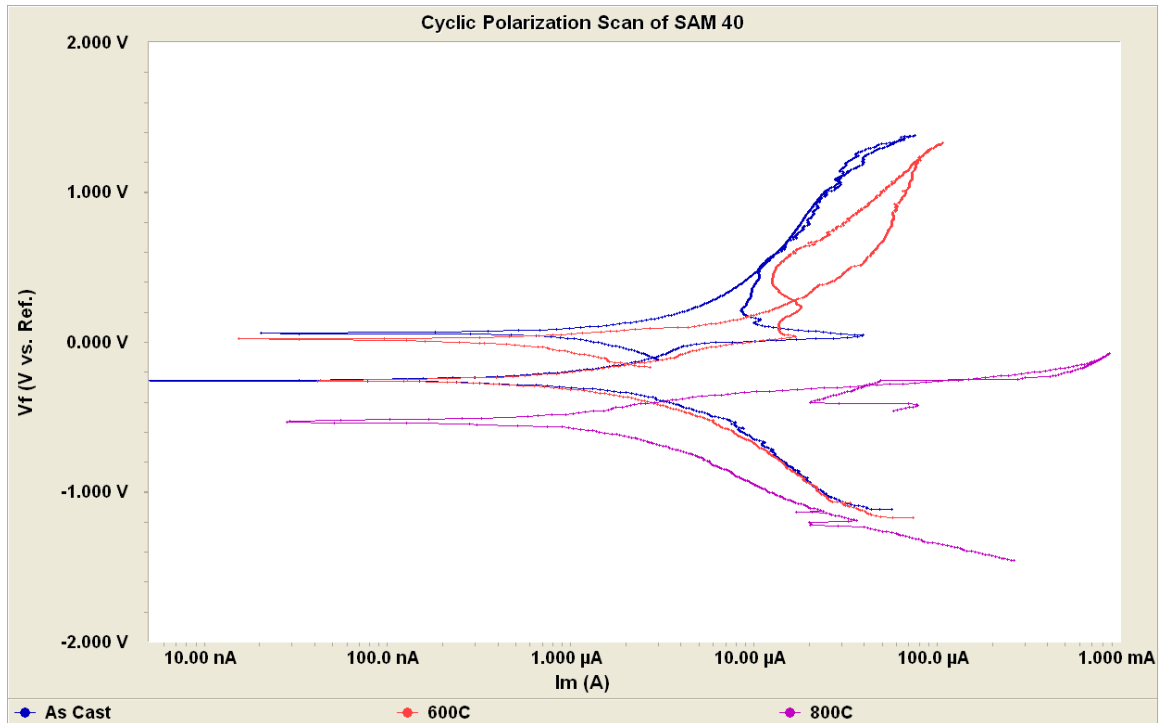


Figure 13. Cyclic polarization measurements for SAM40 base alloy.

## 2. Studies of SAM1X3 and SAM1X7 (Nickel Addition)

SAM1X3 has 3 atomic percent nickel added to base alloy SAM40. Nickel is used in many high strength alloys where corrosion resistance is critical. As potential was increased above the corrosion potential ( $E_{\text{corr}}$ ) of -305mV for the as cast sample (blue), the passive film did not fully break down, which is why it retraced itself. This is very similar to what was seen in the as cast sample of SAM40. Notice that the molybdenum phenomenon did not occur.



The passive film of the sample heat treated to 400 °C (red) started to break down at a lower potential of 540mV and showed a clear repassivation around 10mV (Figure 14). The corrosion potential increased to -229mV. Although the plot for this sample seemed to be offset to the right of the others, this was most likely an effect of different sample size. Nonuniform sample size is an effect of the melt spinning process.

The 700 °C sample (violet) showed similar characteristics to that of the 400 °C sample, but with a slightly higher repassivation potential at 161mV. The  $E_{\text{corr}}$  increased again, this time to -198mV. Thermal exposure did not appear to have reduced the corrosion resistance of this composition as it did on SAM40. The trend of increasing corrosion potential supports this.

Table 5. Electrochemical Measurements for SAM1X3 Alloy

	$E_{\text{corr}}$ (mV)	$E_{\text{pfbd}}$ (mV)	$E_{\text{rp}}$ (mV)
SAM1X3 as cast	-305	1269	NA
SAM1X3-400°C	-229	540	9
SAM1X3-700°C	-198	480	161

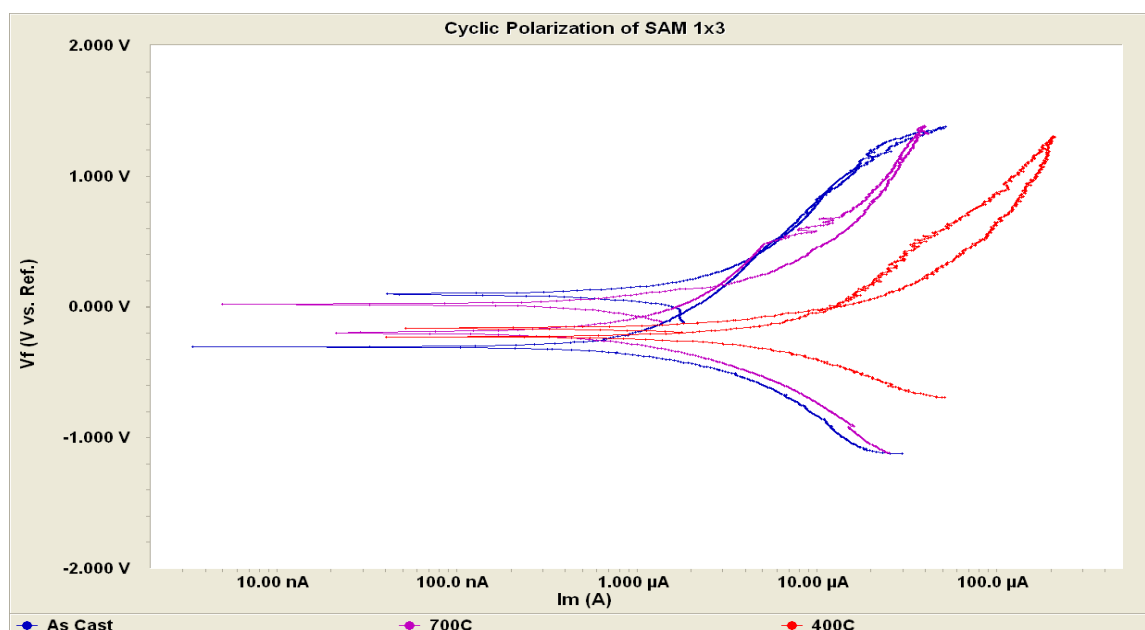


Figure 14. Cyclic polarization studies of SAM1X3 as a function of heat-treatment temperature.

This composition has a 7 atomic % Ni addition to SAM40 base alloy. (SAM1X7) Even the as cast sample (blue, Figure 15) did not appear to be as corrosion resistant as SAM40 or SAM 1X3. The  $E_{\text{corr}}$  was -285mV and, there was a distinctive breakdown of the passive film and a clear repassivation.

The 400 °C (red) sample had a similar break down and a slightly lower repassivation, however its  $E_{\text{corr}}$  was -258mV which was slightly higher than as cast. The 700 °C sample (violet) had a much lower corrosion resistance. The  $E_{\text{corr}}$  dropped significantly to -507mV, the passive film broke down quickly, and current increased as the sample actively corroded. As potential was reversed, the sample appeared to be headed towards a repassivation, but did not make it before the test ends.

Table 6. Electrochemical Measurements for SAM1X7 Alloy.

	$E_{\text{corr}}$ (mV)	$E_{\text{pfbd}}$ (mV)	$E_{\text{rp}}$ (mV)
SAM1X7 as cast	-285	520	120
SAM1X7-400°C	-258	515	-99
SAM1X7-700°C	-507	-18	NA

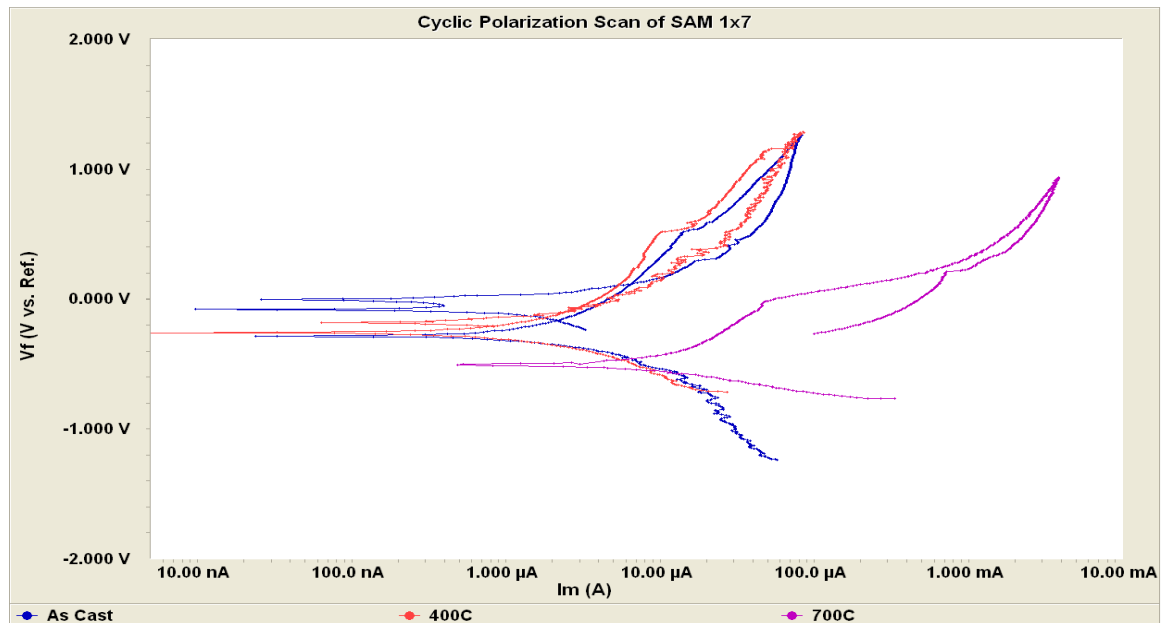


Figure 15. Cyclic polarization studies of SAM1X7 as a function of heat-treatment temperature.

### 3. Studies of SAM3X3 and SAM3X7 (Yttrium Addition)

SAM3X3 has 3 atomic percent of yttrium added to the SAM40 composition. It was expected that yttrium will make the metallic glass more stable since a slightly lower cooling rate is required to cast yttrium containing alloys as a bulk metallic glass.

The as-cast sample (blue, Figure 16) had an  $E_{\text{corr}}$  of -222 mV, which was a slight improvement over SAM40. We see that the passive film did break down at 988 mV and that there was a clear repassivation at 118 mV. The 400 °C sample (red) was slightly less corrosion resistant as is expected. Its repassivation was at a lower potential of 477 mV, and there was a larger difference in current when the potential is reversed. The only improvement was that the  $E_{\text{corr}}$  increased to -204 mV.

The 700 °C sample (violet) showed a higher corrosion resistance than the 400 °C sample. The  $E_{\text{corr}}$  is -202 mV. The passive film broke down at a 963 mV, which was similar to the as cast sample. It had a higher repassivation than the as cast sample at 298 mV. It was not expected that the 700 °C sample would repassivate before the as cast or be more corrosion resistant. This phenomenon was seen again in the next composition of the same family.

Table 7. Electrochemical Measurements for SAM3X3 Alloy.

	$E_{\text{corr}}$ (mV)	$E_{\text{pfbd}}$ (mV)	$E_{\text{rp}}$ (mV)
SAM3x3 as cast	-222	988	118
SAM3x3-400°C	-204	477	-135
SAM3x3-700°C	-202	963	298

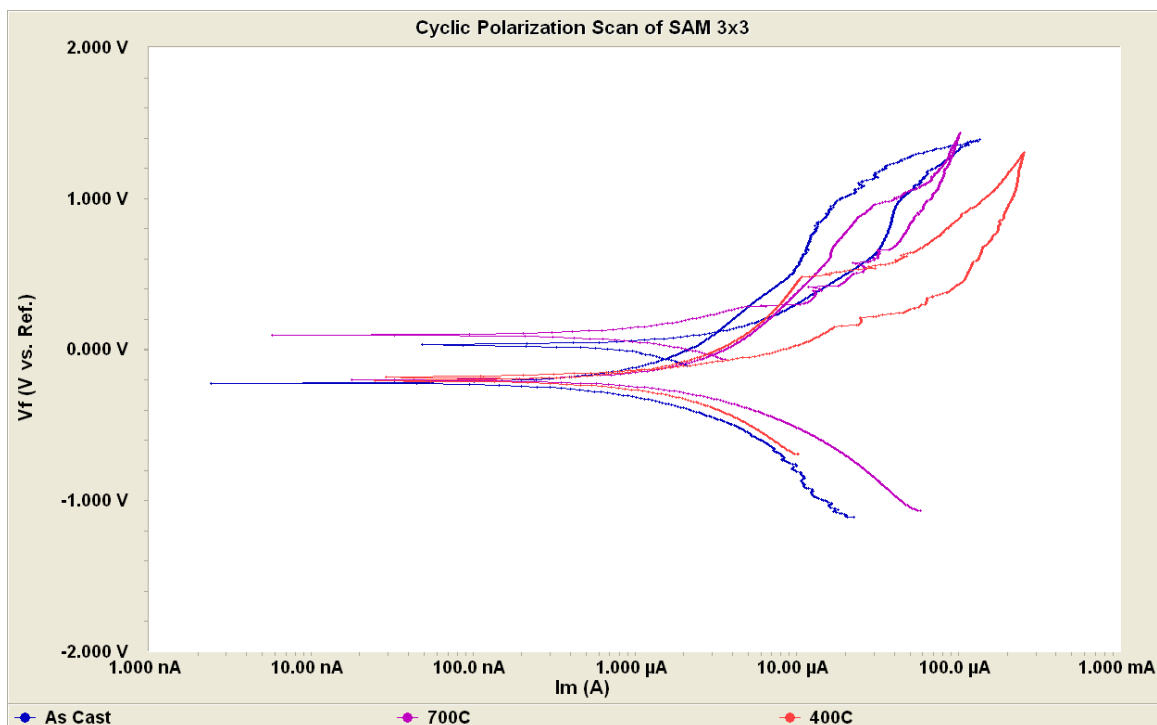


Figure 16. Cyclic polarization studies of SAM3X3 as a function of heat-treatment temperature.

In the as cast sample of SAM3X7 (blue, Figure 17), we saw a similar behavior to the rest of the as cast samples. The  $E_{\text{corr}}$  is -283 mV, which was lower than both SAM3X3 and SAM40. The passive film broke down at 577 mV and there was a clear repassivation at 122 mV. In the 400 °C sample (red), we saw something unique to this testing but very characteristic of cyclic polarization curves. The  $E_{\text{corr}}$  increased to -221 mV, back to the as cast value for SAM3X3. As the passive film broke down at 1.09 V, current increased, but instead of retracing itself at all, this sample had a large hysteresis. Eventually, it repassivated at -191 mV, although this was not very far above the corrosion potential.

The 700 °C sample does something rather unexpected. After the  $E_{\text{corr}}$  at -188 mV, while the potential was increasing, there was no passive film breakdown. As the potential reverses, it retraced itself until current decreases below its initial path. This sample has a much higher resistance to corrosion than the others of this family. Something happened as the sample was heated that made it more corrosion resistant.

The  $E_{\text{corr}}$  of -188 mV was the highest witnessed during experimentation of the samples heat treated to 700 °C. It was the second highest of all the samples at all temperatures. It was suspected that yttrium came out of solution as the sample was heated and collected on the surface. It may well have formed yttrium oxide, which is an extremely stable material and might explain the favorable corrosion behavior.

Table 8. Electrochemical Measurements for SAM3X7 Alloy.

	$E_{\text{corr}}$ (mV)	$E_{\text{pfbid}}$ (mV)	$E_{\text{rp}}$ (mV)
SAM3X7 as cast	-283	577	122
SAM3X7-400°C	-221	NA	-191
SAM3X7-700°C	-188	NA	NA

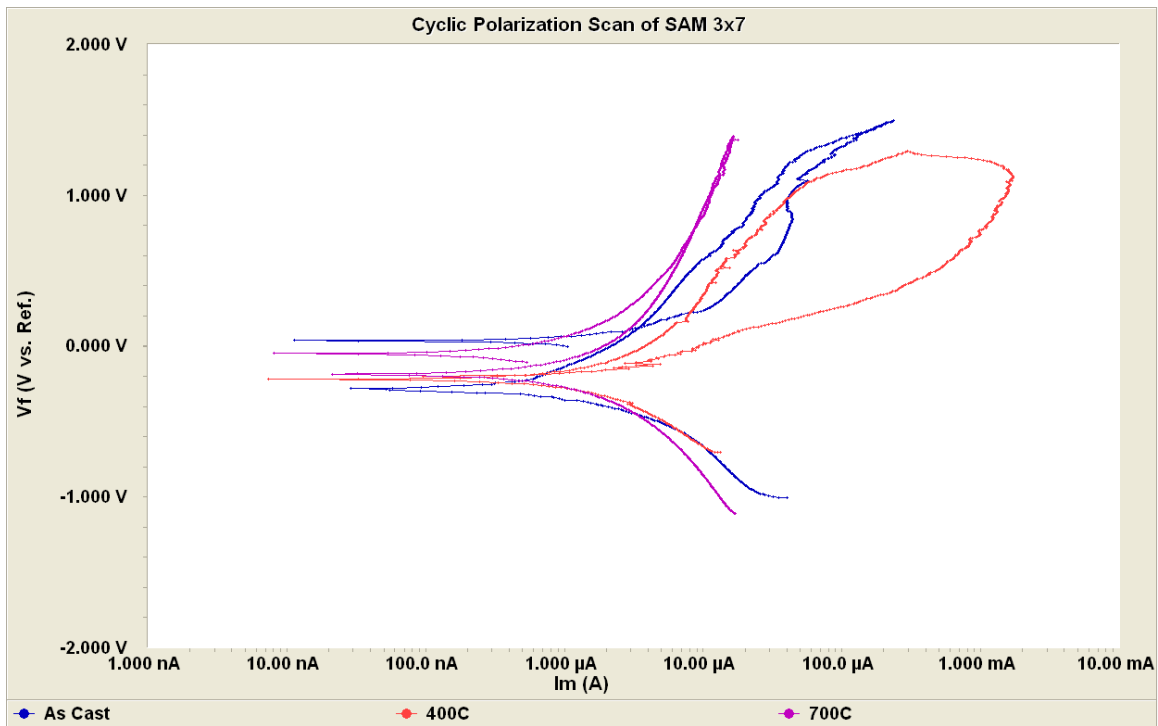


Figure 17. Cyclic polarization studies of SAM3X7 as a function of heat-treatment temperature.

#### 4. Studies of SAM4X3 and SAM4X7 (Titanium Addition)

SAM4X3 has a three atomic percent addition of titanium to the SAM40 composition. The titanium was added with hopes that a protective titanium oxide would form on the surface giving the metallic glass increased corrosion resistance. This was similar to the effect that was suspected in the samples with yttrium addition.

In the as cast sample (blue, Figure 18), after the  $E_{\text{corr}}$  of -241 mV, we saw the phenomenon that was attributed to the corrosion of molybdenum again. When the potential was reversed, the plot retraced itself briefly then the current increased, and finally repassivated at 194 mV. There was no clear passive film break down. The 400 °C sample (red) was similar in the way it imperfectly retraced itself. The  $E_{\text{corr}}$  and repassivations occurred at similar points to the as cast sample at -240 mV and 245 mV respectively.

The 700 °C sample acted similarly to the high temperature SAM40 sample. After the potential increased above the corrosion potential of -303 mV, current increased and the sample corroded actively.

Table 9. Electrochemical Measurements for SAM4X3 Alloy.

	$E_{\text{corr}}$ (mV)	$E_{\text{pfbd}}$ (mV)	$E_{\text{rp}}$ (mV)
SAM4X3 as cast	-241	NA	194
SAM4X3-400°C	-240	NA	245
SAM4X3-700°C	-303	302	NA

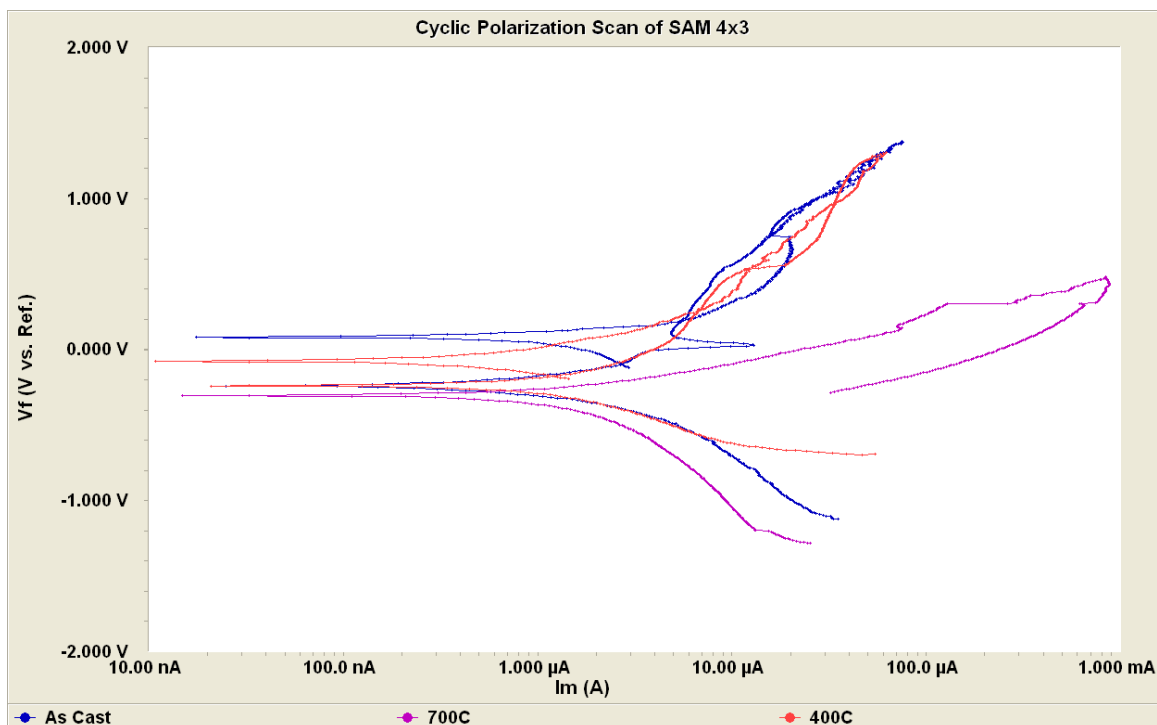


Figure 18. Cyclic polarization studies of SAM4X3 as a function of heat-treatment temperature.

The as cast sample for this composition (blue), again showed the molybdenum phenomenon. The  $E_{\text{corr}}$  was extremely high at -164 mV. The passive film did not fully break down and actually increased in strength as the potential reverses in direction.

In the 400 °C sample (red), the  $E_{\text{corr}}$  decreased to -294 mV. There was a clear passive film breakdown at 520 mV, and we saw a small hysteresis and a repassivation at 125 mV. Although the curve shifted to the right, this again was likely due to a difference in sample size, caused by inconsistencies in the melt spinning process.

Similar to SAM4X3, the 700 °C sample (violet) had a very low corrosion resistance. After the potential increased above the corrosion potential of -203 mV, current increased. There is a small climb right before the passive film broke down and current jumped up again. At this point the sample began to fully actively corrode.

The general trend for adding titanium to SAM40 appeared to be improved corrosion resistance while the material is vitreous. However, once the glass has been exposed to heat the material lost any benefit of the titanium addition.

Table 10. Electrochemical Measurements for SAM4X7 Alloy.

	$E_{\text{corr}}$ (mV)	$E_{\text{pfbd}}$ (mV)	$E_{\text{rp}}$ (mV)
SAM4X7 as cast	-164	966	NA
SAM4X7-400°C	-294	520	125
SAM4X7-700°C	-203	157	NA

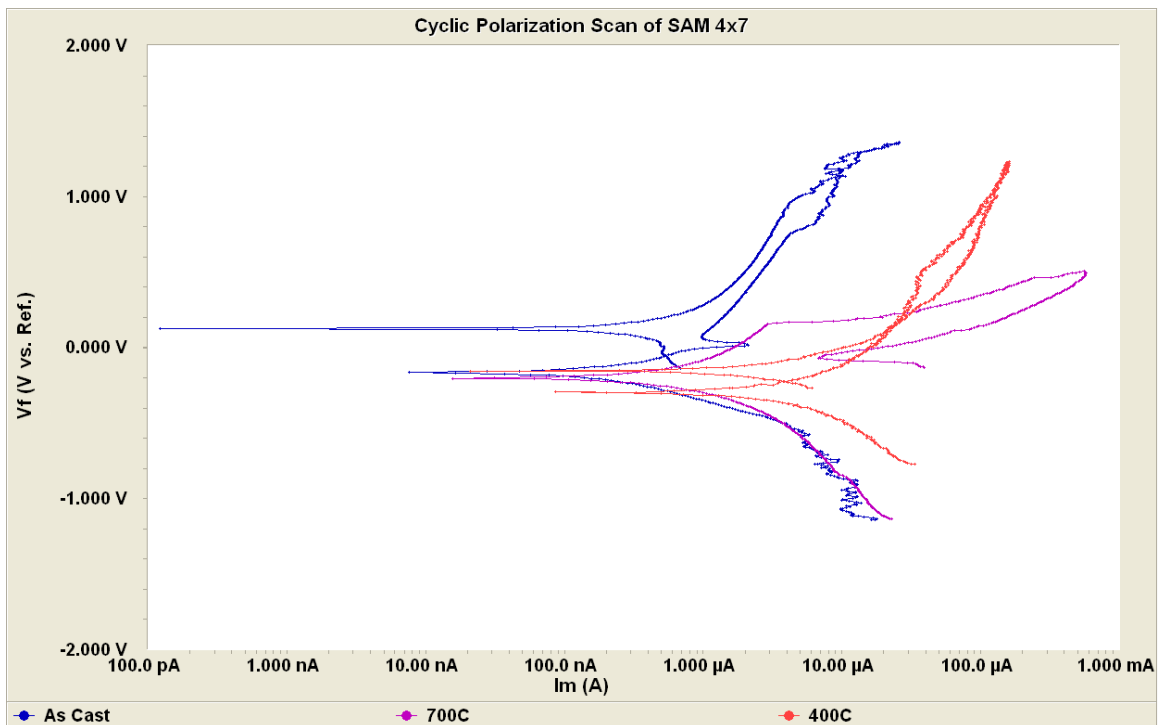


Figure 19. Cyclic polarization studies of SAM4X7 as a function of heat-treatment temperature.

## 5. Summary of Electrochemical Results

Table 11 shows the effects of the alloy additions on the three parameters: corrosion potential, passive film breakdown potential, and repassivation potential. These values do not independently state the quality of a sample's corrosion resistance. They



only quantify their representative parameters. The shapes seen in the curves significantly and effectively demonstrate the behavior of the material in a corrosive environment.

The green highlighted blocks show compositions for which the passive film remained stable and the sample demonstrated relatively good corrosion resistance. The red highlighted blocks show compositions for which the passive film broke down completely and the sample actively corroded. The samples heat treated to 700°C of SAM40, SAM1X7 (nickel addition), SAM4X3 (titanium addition), and SAM4X7 (titanium addition) all had similar results. The passive film destabilized and broke down allowing the material to actively corrode. The difference between these samples heat treated to 700°C and the samples heat treated to temperatures less than the glass transition temperature ( $T_g$ ) of the same alloy is the devitrification. At the higher temperatures, crystalline phases were formed that are potential nucleation sites for corrosion. It is probable that these specific, crystalline phases were less corrosion resistant or that the amount of crystalline phases present was enough to negate the effects of the amorphous microstructure. Regardless, the result was the same; these alloys demonstrated poor corrosion resistance when exposed to high temperatures.

The samples heat treated to 700°C of SAM1X3 (nickel addition) and SAM3X3 (yttrium addition) had passive films that began to destabilize, but did not completely break down. As the potential started to decrease, the passive film recovered and became stable enough so that the rate of corrosion decreased. We call the passive film recovery a repassivation. These two alloys had compositions that were stable enough to either not devitrify to an extent where the benefit of the amorphous microstructure was lost or produce phases that were themselves corrosion resistant.

The sample heat treated to 700°C of SAM3X7 (7 atomic % Y addition) was unique in the fact that it was the only sample heat treated above the glass transition temperature where the passive film did not destabilize at all. Based on the presence of a small peak in the x-ray diffraction scan, it seems likely that crystalline phases were present to some extent in the microstructure of this material. There are two possibilities why this alloy demonstrated such magnificent corrosion resistance. One possibility is

that the yttrium addition improved the stability of the amorphous microstructure. Although the glass transition temperature was not clear for this specific alloy, it does have the highest predicted crystallization temperature of all the alloys tested at 697°C as shown in Table 2. Another possibility is that a relatively large amount of yttrium concentrated on the surface to some degree and formed a yttrium oxide layer ( $\text{Y}_2\text{O}_3$ ). Yttrium oxide is a passive film known to be extremely stable. Formation of such a protective layer on the surface of these iron-based metallic glasses could enable them to have even greater corrosion resistance than previously demonstrated. It is also possible that a combination of the protective yttrium oxide layer and a highly stable microstructure both led to unprecedented performance of SAM3X7.

Based on what has been learned, it is now possible to qualitatively assign values to the weighting coefficients A, B, and C for the modified PREN equation. (Equation 3) The coefficient A corresponds to nickel. Since nickel showed no substantial improvement to the corrosion resistance, its value would be approximately zero. The coefficient B, belonging to yttrium, would be assigned a higher positive value. Although the relative benefit of adding yttrium compared to chromium, tungsten, or molybdenum is uncertain, we do know that yttrium addition does have a positive effect. The coefficient C, corresponding to titanium, would be assigned a slightly negative value. It did not improve the corrosion resistance and likely degraded it.

Table 11. Summary of Electrochemical Results.

	Ecorr (mV)	Epfbd (mV)	Erp (mV)
SAM40 as cast	-251.4	1282	NA
SAM40-600°C	-258.2	626.4	271.6
SAM40-800°C	-525.6	-360.8	NA
SAM1X3 as cast	-305.1	1269	NA
SAM1X3-400°C	-228.5	540	8.74
SAM1X3-700°C	-198.4	480	161.3
SAM1X7 as cast	-284.7	520	120.1
SAM1X7-400°C	-258.1	515	-98.6
SAM1X7-700°C	-507.3	-17.7	NA
SAM3X3 as cast	-221.8	NA	118
SAM3X3-400°C	-204.2	477.2	-134.5
SAM3X3-700°C	-201.5	NA	298.3
SAM3X7 as cast	-282.6	577	122.2
SAM3X7-400°C	-221.2	1090	-191.3
SAM3X7-700°C	-188.3	NA	NA
SAM4X3 as cast	-240.7	NA	193.9
SAM4X3-400°C	-240	470	244.6
SAM4X3-700°C	-303.2	301.5	NA
SAM4X7 as cast	-163.6	965.9	NA
SAM4X7-400°C	-294.4	520.2	125.2
SAM4X7-700°C	-203	156.6	NA

THIS PAGE INTENTIONALLY LEFT BLANK

## VI. CONCLUSIONS

The objective of this thesis was to analyze the effect of nickel, yttrium, and titanium additions upon the recrystallization temperature, amorphous microstructure, and corrosion resistance of the iron-based bulk metallic glass SAM40 base alloy

Nickel did not noticeably improve the corrosion resistance or microstructure stability of SAM40 base alloy. The nickel addition sample SAM1X3, with a three atomic percent addition, heat treated to 700°C showed a slight improvement over SAM40 base alloy. The passive film did not break down in the same way that was seen in the high temperature sample of SAM40.  $E_{\text{corr}}$  and  $E_{\text{pfbid}}$  decreased for the as cast sample.

The yttrium addition had a much better effect than the Nickel. From the XRD analysis we see that the intensity of the peaks were much lower for the yttrium addition samples than for any of the other alloy additions. This demonstrates that the hypothesis that yttrium will improve the stability of the microstructure is correct. Not only did yttrium improve the stability of the amorphous microstructure, it also improved the corrosion resistance as it is heated. This suggests that a stronger passive film is forming on the surface as the material is heat treated to higher temperatures. One possibility is that yttrium oxide, which is highly stable and corrosion resistant, is forming during the heat treatment.

The titanium addition did not improve the corrosion resistance of SAM40 base alloy. The XRD analysis shows that the stability of the amorphous microstructure was negatively affected by the titanium addition. The cyclic polarization confirmed the negative effects of the titanium. Both SAM4X3 and SAM4X7 corroded actively when heat treated to 700°C. One good thing that can be said about the titanium addition is that the as cast samples did not show a negative effect. The  $E_{\text{corr}}$  were higher for both SAM4X3 and SAM4X7 than SAM40 base alloy.

THIS PAGE INTENTIONALLY LEFT BLANK

## **VII. RECOMMENDATIONS FOR FUTURE RESEARCH**

There is great room for future exploration in the field of bulk metallic glasses. There are limitless possibilities for applications of these materials. As our knowledge and understanding of these materials grows, compositions can be adapted to the specific needs of each application.

Specifically for the additions of yttrium, nickel, and titanium, more research needs to be done in quantifying characteristics of these materials. Finer intervals in annealing temperature will show whether devitrification occurs at a specific temperature or over a large range. The correlation between exposure to heat and corrosion rate can also be better defined. In addition, BMGs are, by definition, metastable materials. It will be important to do a kinetics study of crystallization for key temperatures of interest. Prolonged exposure at temperature may result in crystallization not observed after only one hour.

In the case of yttrium, further research will need to be done to determine the optimum yttrium composition to achieve the needed corrosion resistance and amorphous microstructure stability for the specific application. It will be important to identify the phases and mechanisms responsible for its enhanced corrosion resistance. Electron microscopy should be able to provide combined compositional crystallographic and compositional information that could identify the individual phases that have formed.

THIS PAGE INTENTIONALLY LEFT BLANK



## LIST OF REFERENCES

- Caltech. "Professor William L. Johnson." Caltech.  
<http://www.its.caltech.edu/~vitreloy/index.htm>, (accessed June 6, 2011).
- Computational Thermodynamics. Gibbs Phase Rule. CALPHAD.  
[http://www.calphad.com/gibbs\\_phase\\_rule.html](http://www.calphad.com/gibbs_phase_rule.html) (accessed June 12, 2011).
- Farmer, J. C., J. J. Haslam, S. D. Day, D. J. Branagan, C. A. Blue, J. D. K. Rivard, L. F. Aprigliano, N. Yang, J. H. Perepezko, and M. B. Beardsley. 2005. Corrosion Characterization of Iron-Based High-Performance Amorphous Metal Thermal-Spray Coatings. Paper presented at ASME PVP: Pressure Vessels and Piping Division Conference, July 17–21, Denver, Colorado.
- Farmer, Joseph C. 2005. High Performance Corrosion Resistant Material Project's New Iron-Based Amorphous Metal Coatings: Enhanced Corrosion Performance and Substantial Cost Savings. Presentation at Nuclear Waste Technical Review Board, November 16, Washington DC.
- . 2008. High Performance Corrosion Resistant Materials: Fe Based Amorphous Metal Coatings and Composite Surfaces. Encyclopedia of Composites LLNL Book 462191.
- . 2010. "High Performance Corrosion Resistant Materials: Fe Based Amorphous Metal Coating and Composite Surfaces." Encyclopedia of Composites LLNL BOOK 462191.
- Kaufman, Larry. 2004. Calculation of Coating Composites for Use in Various Corrosive Environments with Pourbaix and Thermal Stability Diagrams. High Performance Corrosion Resistant Materials Final Report.
- Liquidmetal Technologies. "Metallic glass: A Drop of the Hard Stuff." Liquidmetal Technologies. <http://www.liquidmetal.com/news/dsp.news.04x105.asp> (accessed March 15, 2011).
- Pourbaix, M. 1974. Atlas of Electrochemical Equilibria in Aqueous Solutions. Houston: NACE International and Cebelcor.
- Xu, Jian, Xinde Bai, Yundian Fan, Wenliang Liu, and Hongbin Bei. 2000. Journal of Materials Science 35: 6225–6229.
- Yang, Nancy, Joseph C. Farmer, G. Lucadamo, T. Headley, and D. Days. 2005. Devitrification and Its Influence on Corrosion Performance of SAM2x5 and SAM 1651. High Performance Corrosion Resistant Materials Annual Report.

THIS PAGE INTENTIONALLY LEFT BLANK

## APPENDIX

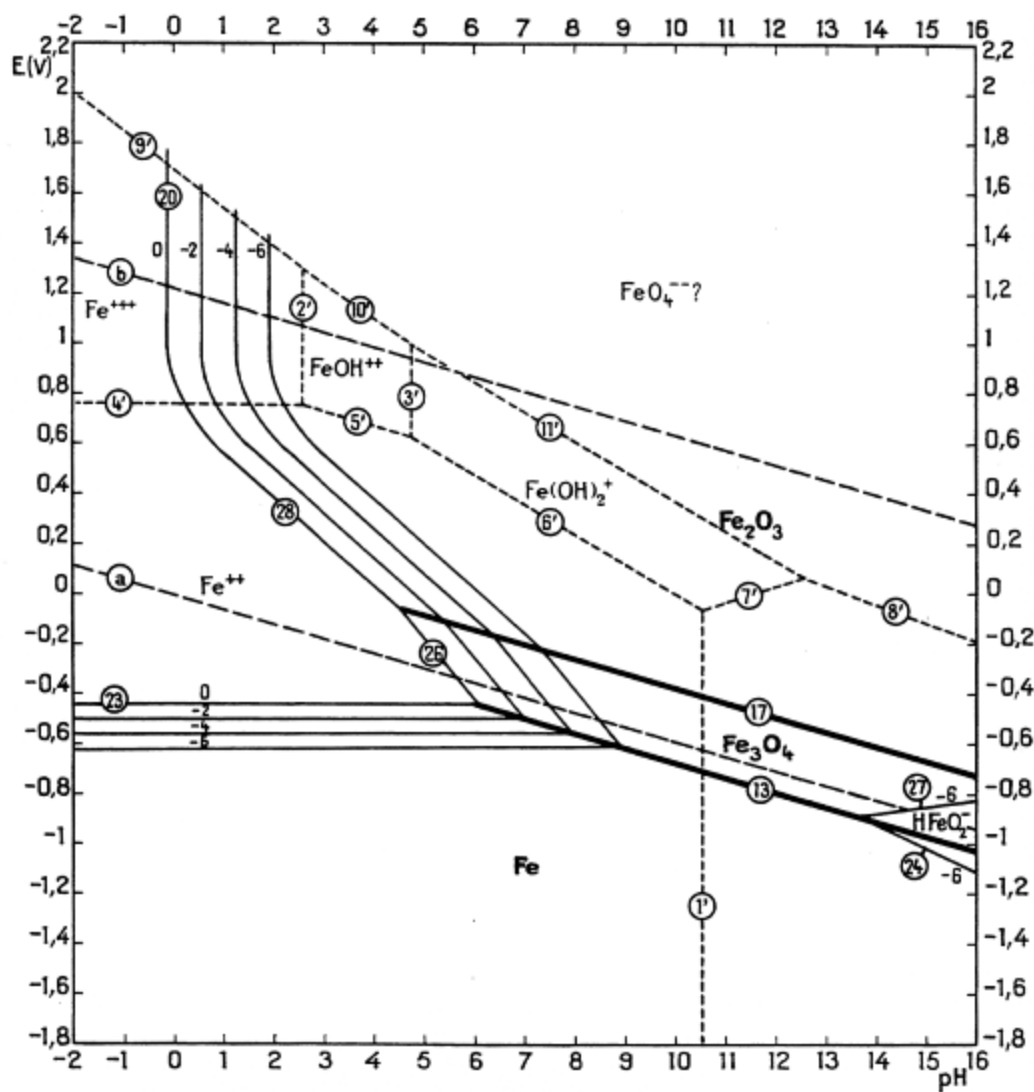


Figure 20. Pourbaix Diagram for Iron (Fe).<sup>25</sup>

<sup>25</sup> M. Pourbaix, Atlas of Electrochemical Equilibria in Aqueous Solutions (Houston: NACE International and Cebalcor, 1974).

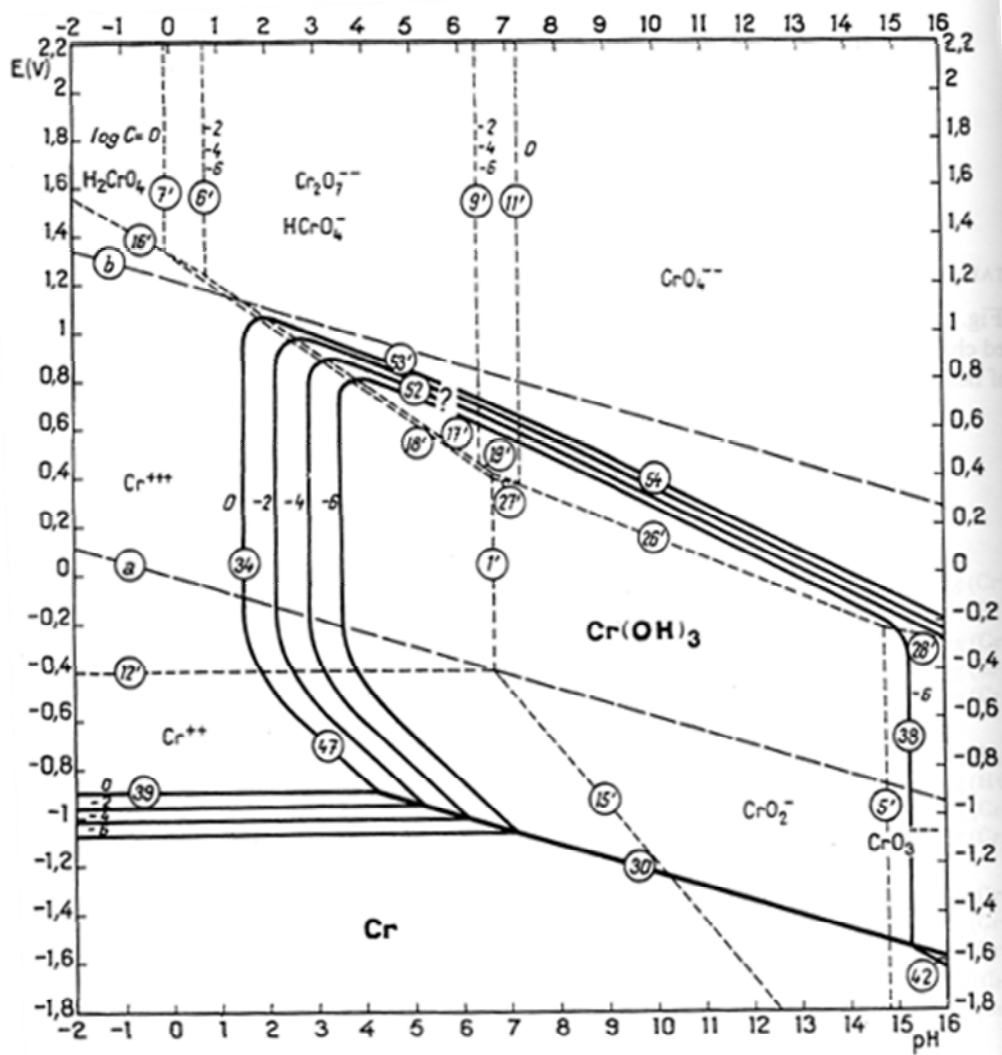


Figure 21. Pourbaix Diagram for Chromium (Cr).<sup>26</sup>

<sup>26</sup> M. Pourbaix, Atlas of Electrochemical Equilibria in Aqueous Solutions (Houston: NACE International and Cebelcor, 1974).

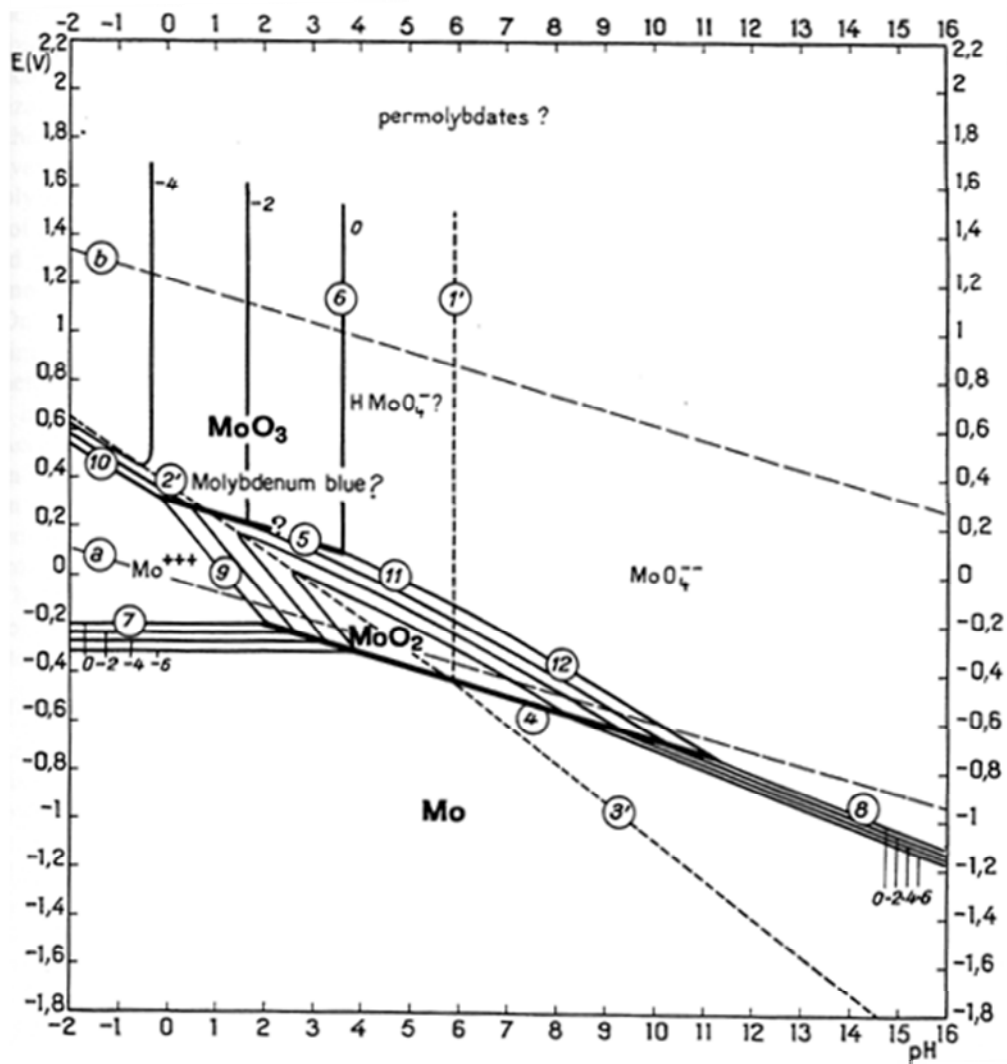


Figure 22. Pourbaix Diagram for Molybdenum (Mo).<sup>27</sup>

<sup>27</sup> M. Pourbaix, Atlas of Electrochemical Equilibria in Aqueous Solutions (Houston: NACE International and Cebalcor, 1974).

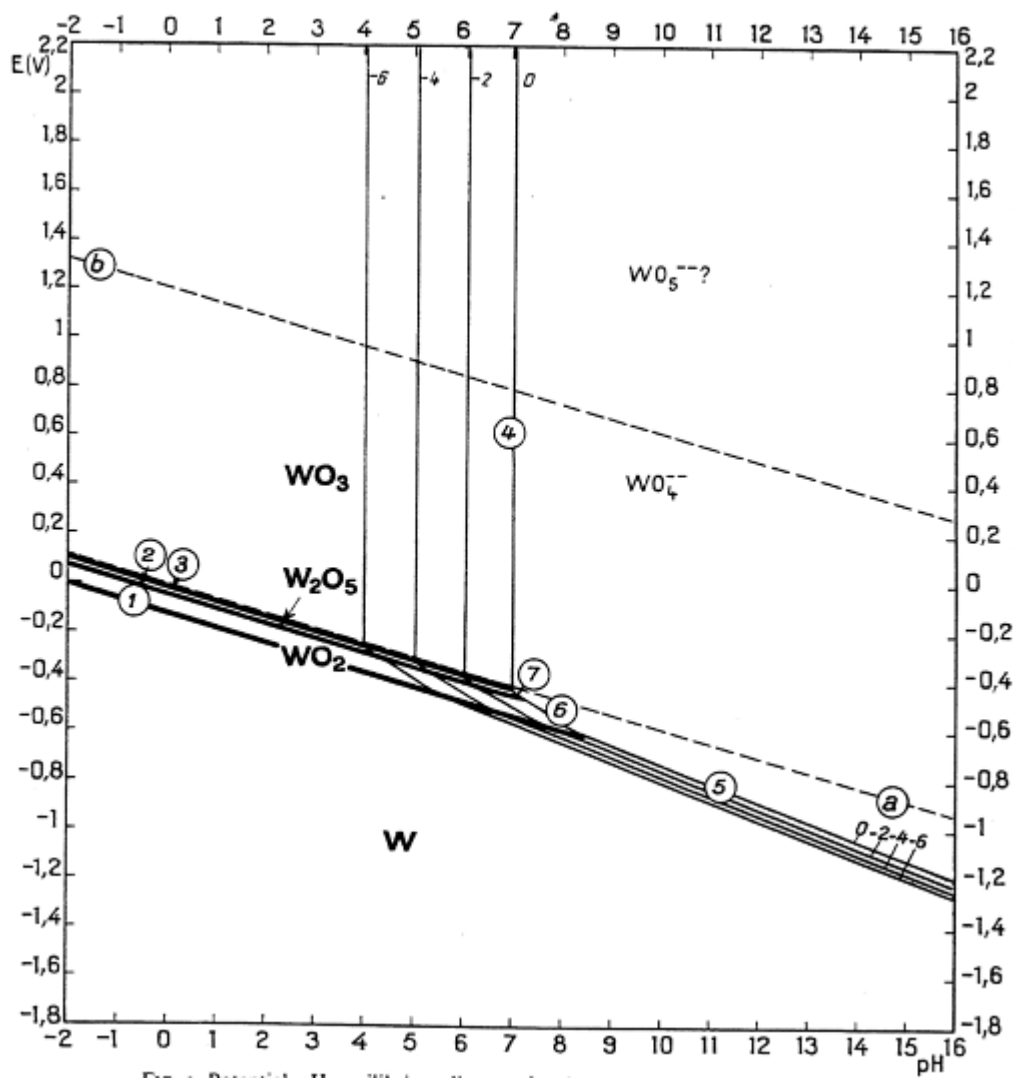


Figure 23. Pourbaix Diagram for Tungsten (W).<sup>28</sup>

<sup>28</sup> M. Pourbaix, Atlas of Electrochemical Equilibria in Aqueous Solutions (Houston: NACE International and Cebelcor, 1974).

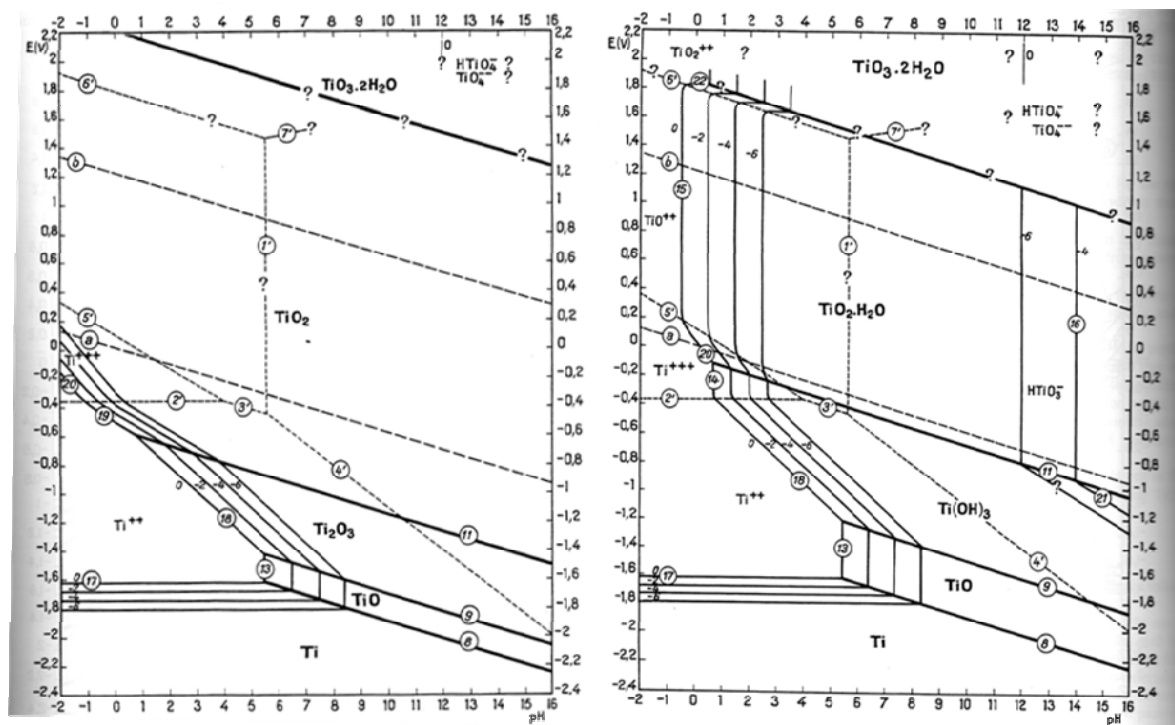


Figure 24. Pourbaix Diagrams for Titanium.<sup>29</sup>

<sup>29</sup> M. Pourbaix, Atlas of Electrochemical Equilibria in Aqueous Solutions (Houston: NACE International and Cebelcor, 1974).

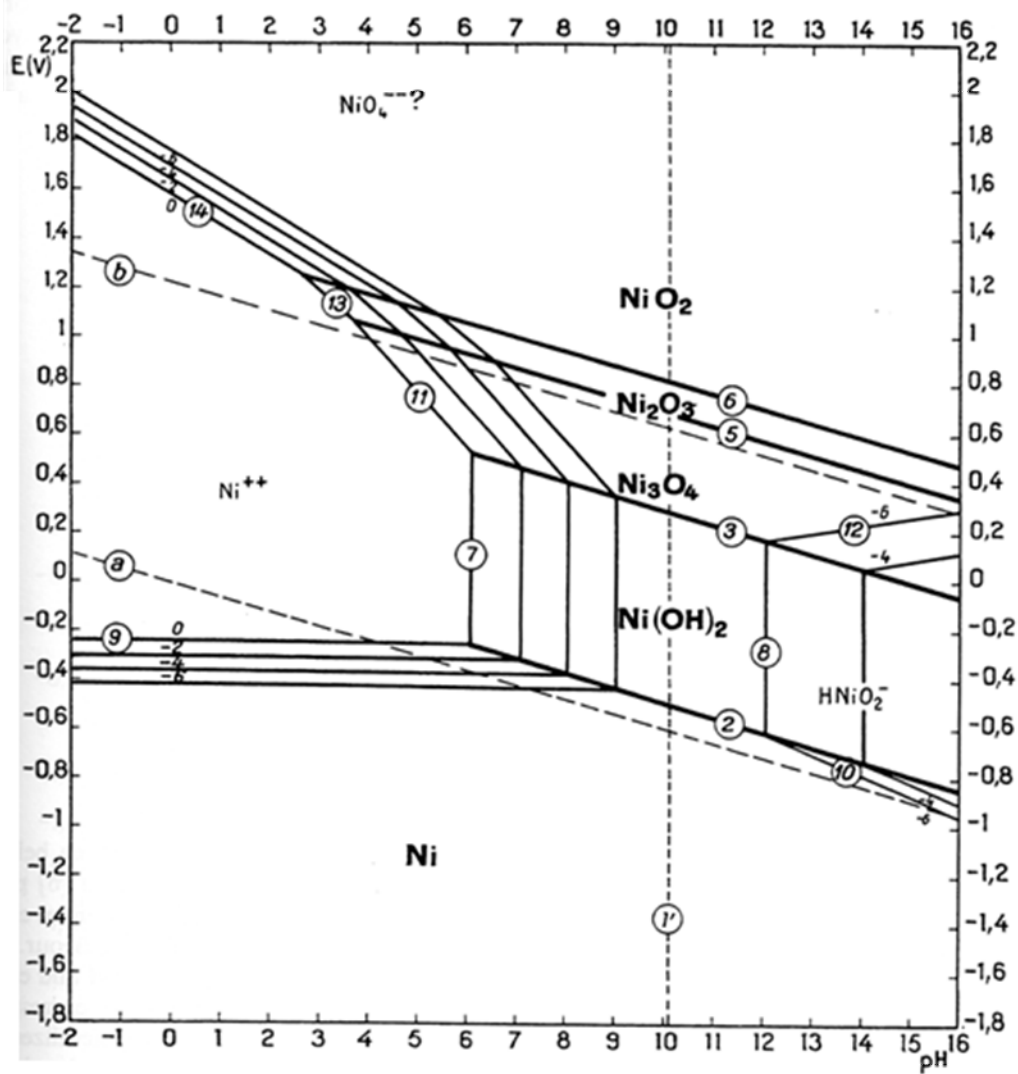


Figure 25. Pourbaix Diagram for Nickel (Ni).



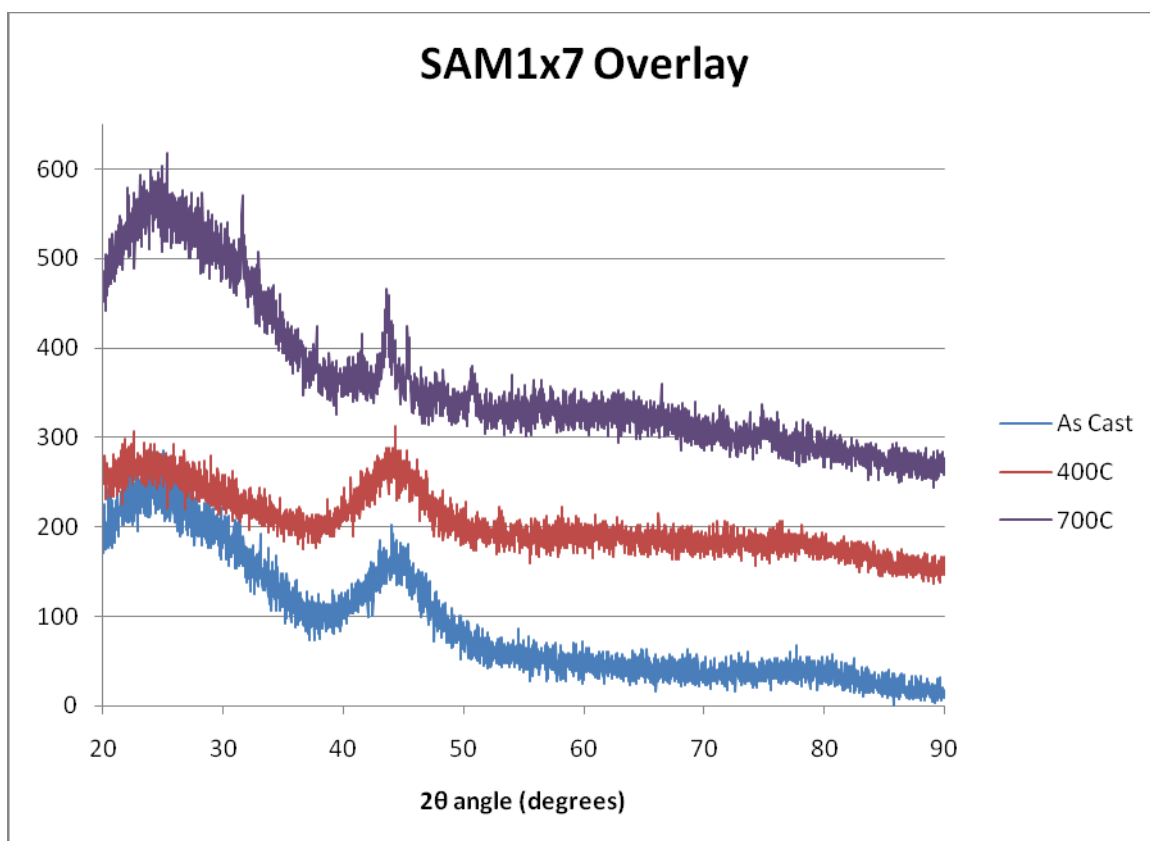


Figure 26. Overlay of SAM1X7 XRD scans as cast, heat treated to 400°C, and heat treated to 700°C.

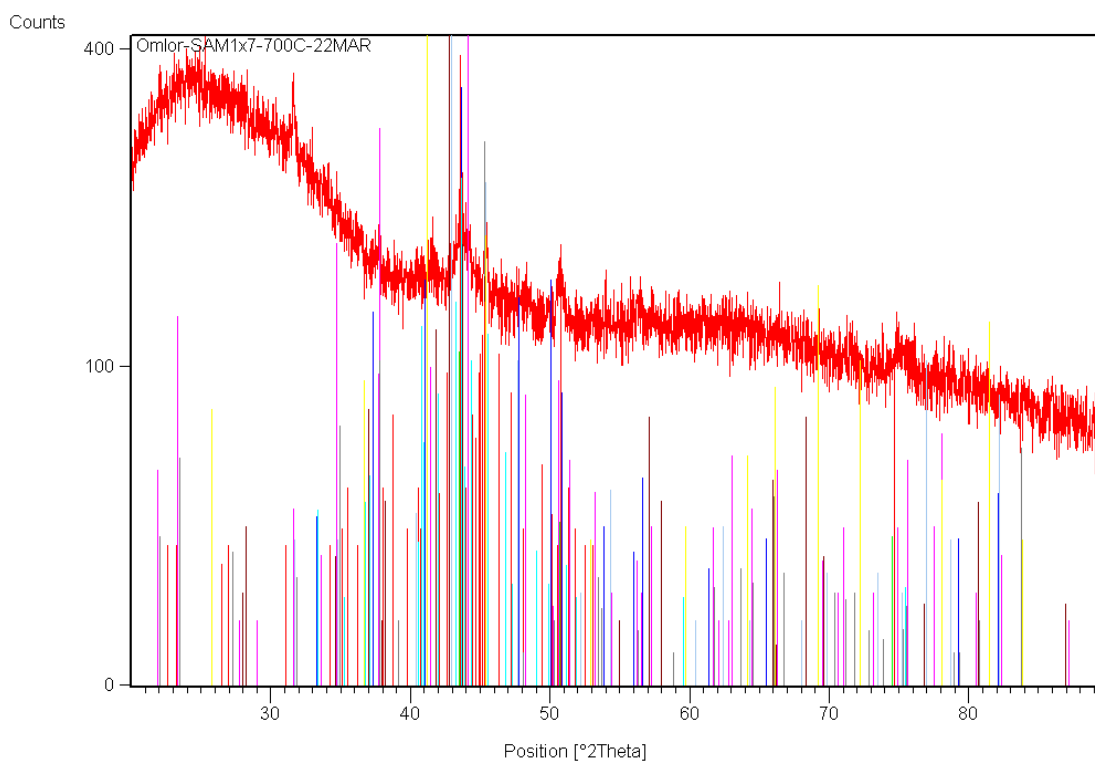


Figure 27. Plot of XRD peaks of possible phases in SAM1X7.

No.	Visi...	Ref. Code	Compoun...	Chemical For...	Sc...	Scal...	Sem...
1	<input checked="" type="checkbox"/>	00-047-1...	Iron Nickel	Fe <sub>0.64</sub> Ni <sub>0.36</sub>	29	0.942	-
2	<input checked="" type="checkbox"/>	00-044-1...	martensite	C <sub>0.12</sub> Fe <sub>1.88</sub>	16	0.461	-
3	<input checked="" type="checkbox"/>	00-047-1...	awaruite	(Fe, Ni)	15	0.264	-
4	<input checked="" type="checkbox"/>	00-045-1...	Iron Silicon	Fe <sub>3</sub> Si	14	0.699	-
5	<input checked="" type="checkbox"/>	00-022-0...	Fersilicite, ...	Fe Si	9	0.396	-
6	<input checked="" type="checkbox"/>	00-012-0...	Awaruite	(Ni, Fe)	5	0.113	-
7	<input checked="" type="checkbox"/>	00-001-1...	Boron Car...	B <sub>4</sub> C	3	0.734	-
8	<input checked="" type="checkbox"/>	00-001-1...	Chromium	Cr	3	0.625	-
9	<input checked="" type="checkbox"/>	00-024-0...	Manganes...	Mn <sub>0.815</sub> Si <sub>0.1...</sub>	4	0.579	-
10	<input checked="" type="checkbox"/>	00-047-1...	Boron Iron	B <sub>6</sub> Fe <sub>23</sub>	10	0.848	-
11	<input checked="" type="checkbox"/>	00-020-1...	Tungsten ...	W <sub>2</sub> C	0	0.000	-
12	<input checked="" type="checkbox"/>	00-035-0...	carbon tetr...	B <sub>4</sub> C	2	0.250	-
13	<input checked="" type="checkbox"/>	00-037-0...	Iron Carbide	Fe <sub>2</sub> C	1	1.767	-
14	<input checked="" type="checkbox"/>	00-047-1...	Molybden...	Mo <sub>1.24</sub> Ni <sub>0.76</sub>	6	0.610	-
15	<input checked="" type="checkbox"/>	00-035-0...	Chromium ...	Cr <sub>23</sub> C <sub>6</sub>	3	1.968	-
16	<input checked="" type="checkbox"/>	00-051-0...	Molybden...	Mo <sub>3</sub> Si	2	1.010	-

Figure 28. List of possible phases in SAM1X7.

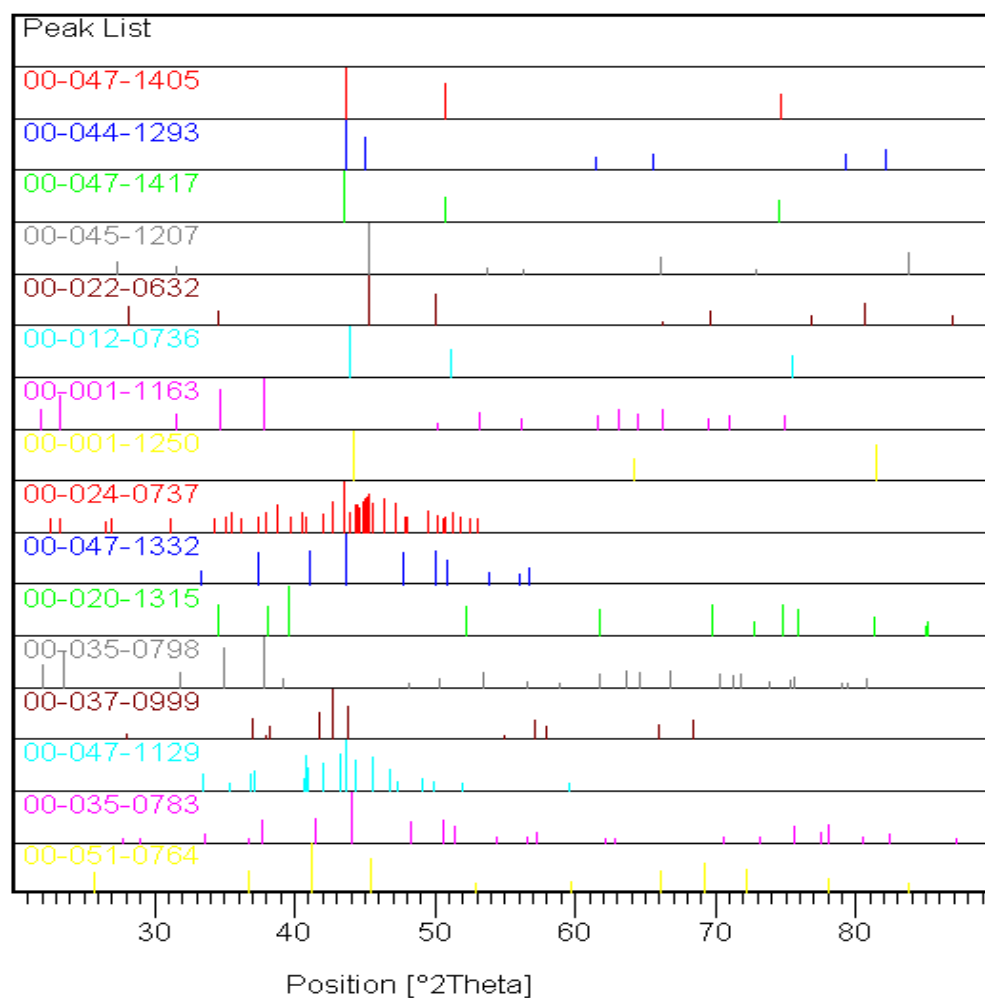


Figure 29. Plot of XRD peaks of possible phases in SAM1X7.

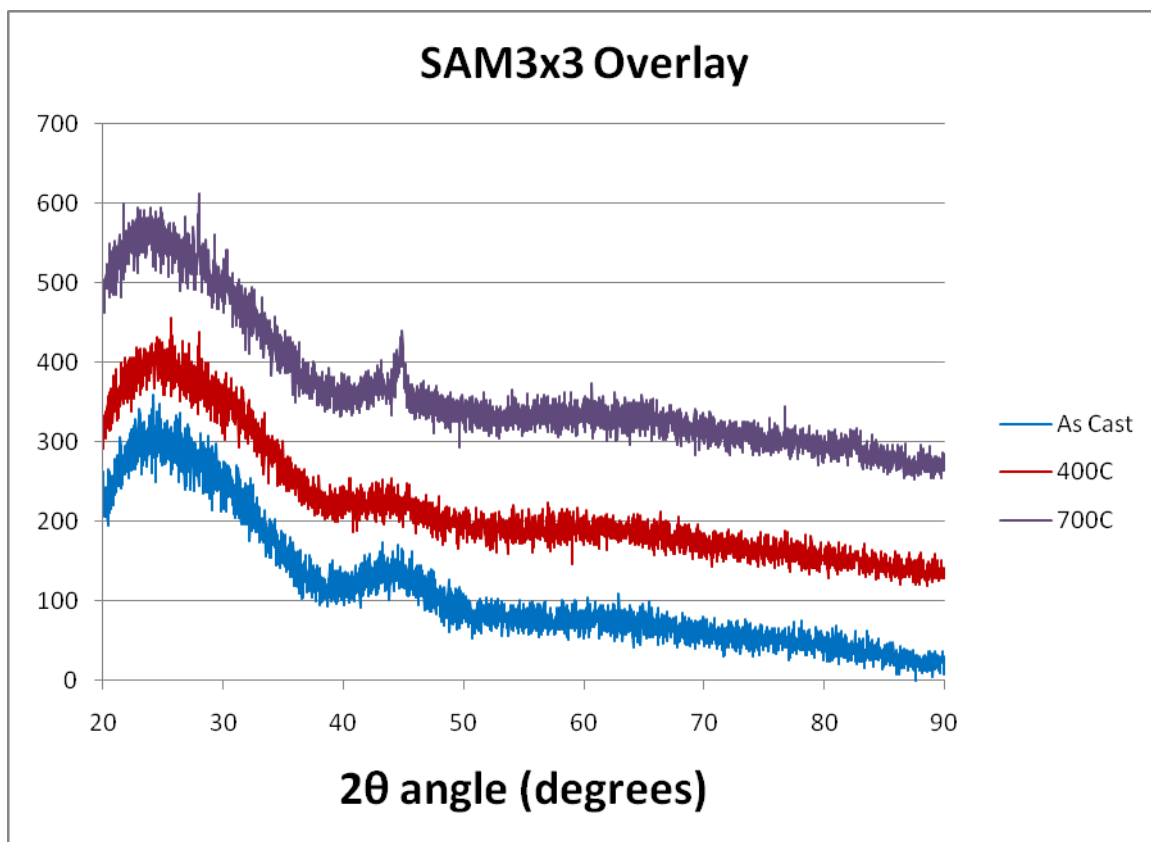


Figure 30. Overlay of SAM3X3 XRD scans as cast, heat treated to 400°C, and heat treated to 700°C.

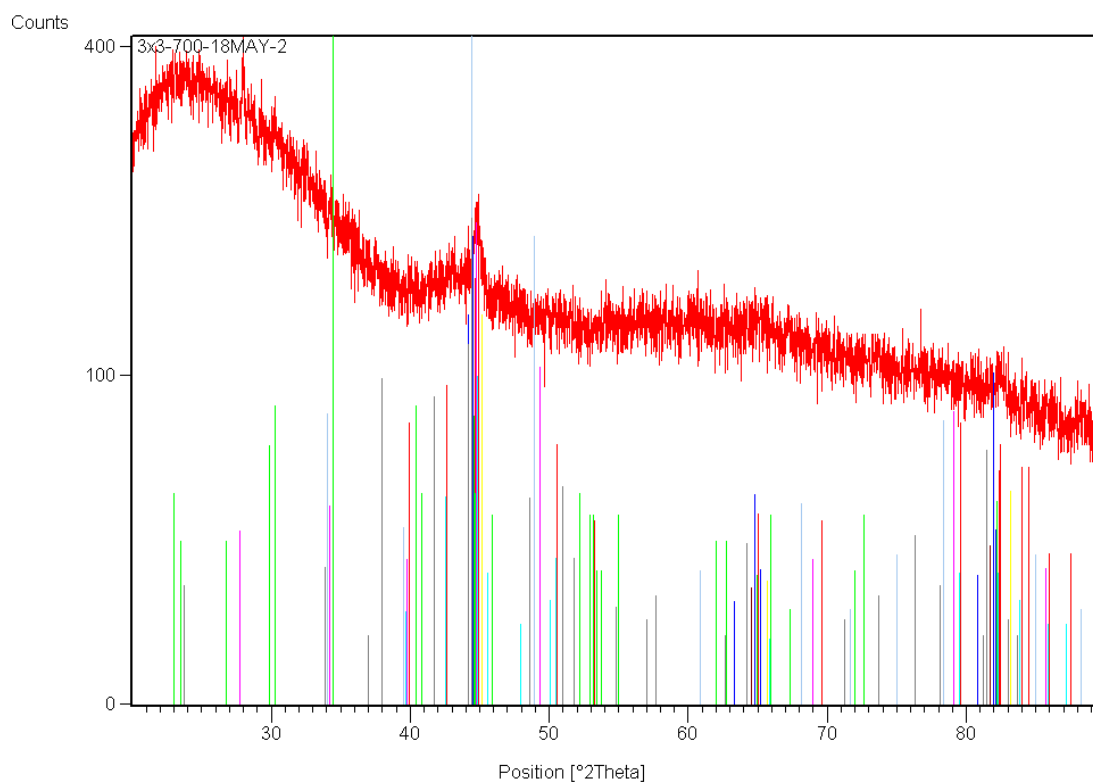


Figure 31. Plot of XRD peaks of possible phases in SAM3X3.

No.	Visi...	Ref. Code	Compoun...	Chemical For...	Sc...	Scal...	Sem...
1	<input checked="" type="checkbox"/>	00-006-0...	bainite, fer...	Fe	15	0.407	-
2	<input checked="" type="checkbox"/>	00-044-1...	martensite	C0.055 Fe1.945	12	0.340	-
3	<input checked="" type="checkbox"/>	00-054-0...	410-L Stai...	Fe - Cr	9	0.186	-
4	<input checked="" type="checkbox"/>	00-001-1...	Chromium	Cr	6	0.290	-
5	<input checked="" type="checkbox"/>	00-006-0...	Chromium...	Cr	6	0.189	-
6	<input checked="" type="checkbox"/>	00-017-0...	Iron Carbide	Fe7 C3	6	0.241	-
7	<input checked="" type="checkbox"/>	00-050-1...	â-Si5 C3	Si5 C3	5	0.520	-
8	<input checked="" type="checkbox"/>	00-035-0...	Suessite	Fe3 Si	5	0.341	-
9	<input checked="" type="checkbox"/>	00-006-0...	Iron Carbide	Fe C	4	0.507	-
10	<input checked="" type="checkbox"/>	00-034-0...	434-L stain...	Fe - Cr	3	0.492	-
11	<input checked="" type="checkbox"/>	00-011-0...	Silicon Yttr...	Y Si2	0	2.776	-
12	<input checked="" type="checkbox"/>	00-028-0...	Manganes...	Mn23 C6	3	0.530	-
13	<input checked="" type="checkbox"/>	00-042-1...	Manganes...	Mn Si	3	0.200	-

Figure 32. List of possible phases in SAM3X3.

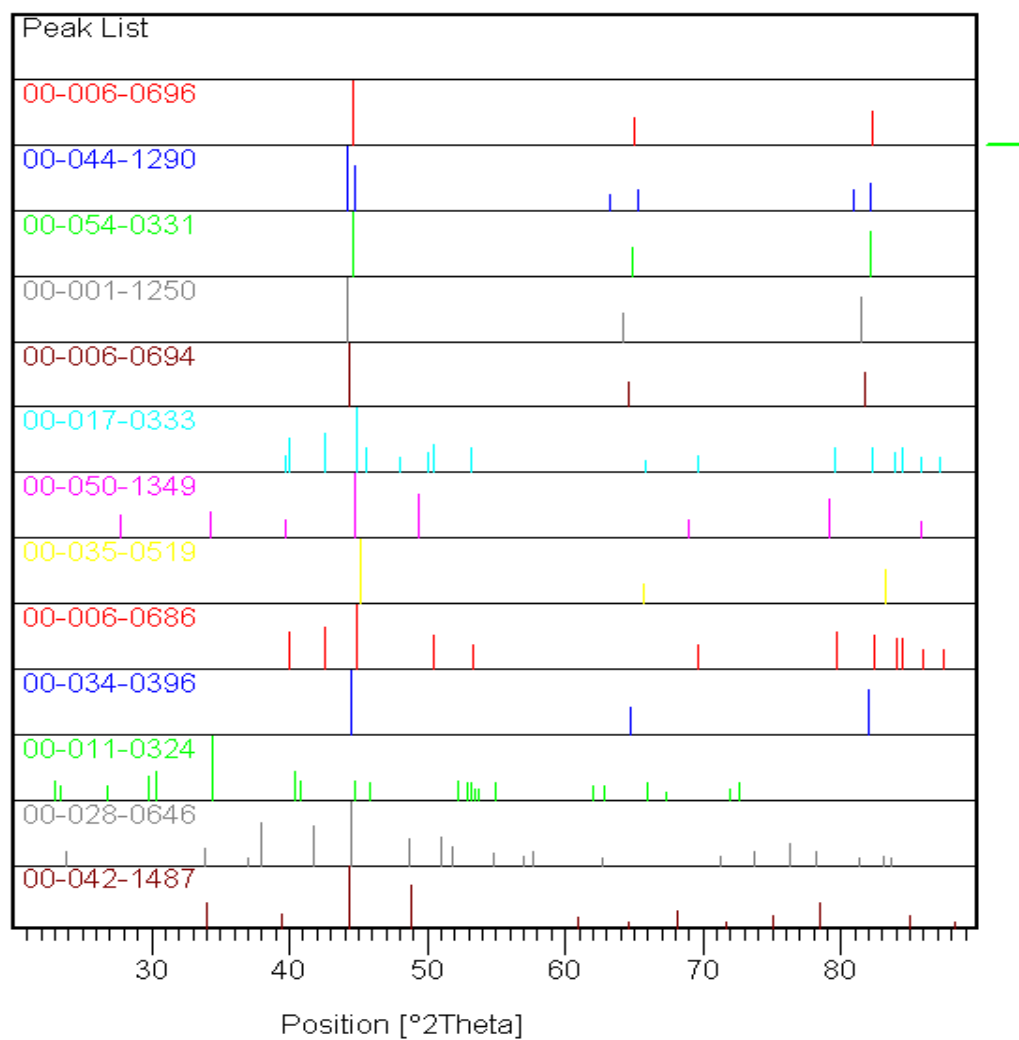


Figure 33. Plot of XRD peaks of possible phases in SAM3X3.

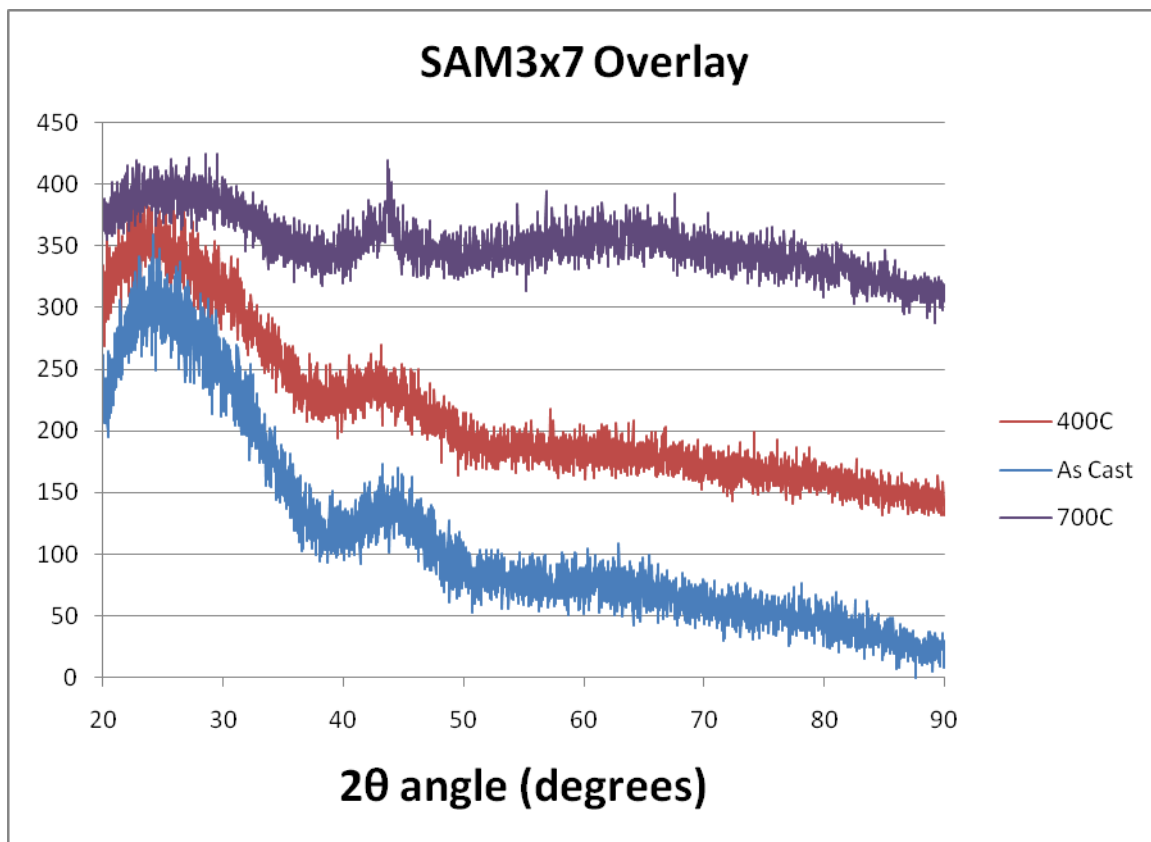


Figure 34. Overlay of SAM3X7 XRD scans as cast, heat treated to 400°C, and heat treated to 700°C.

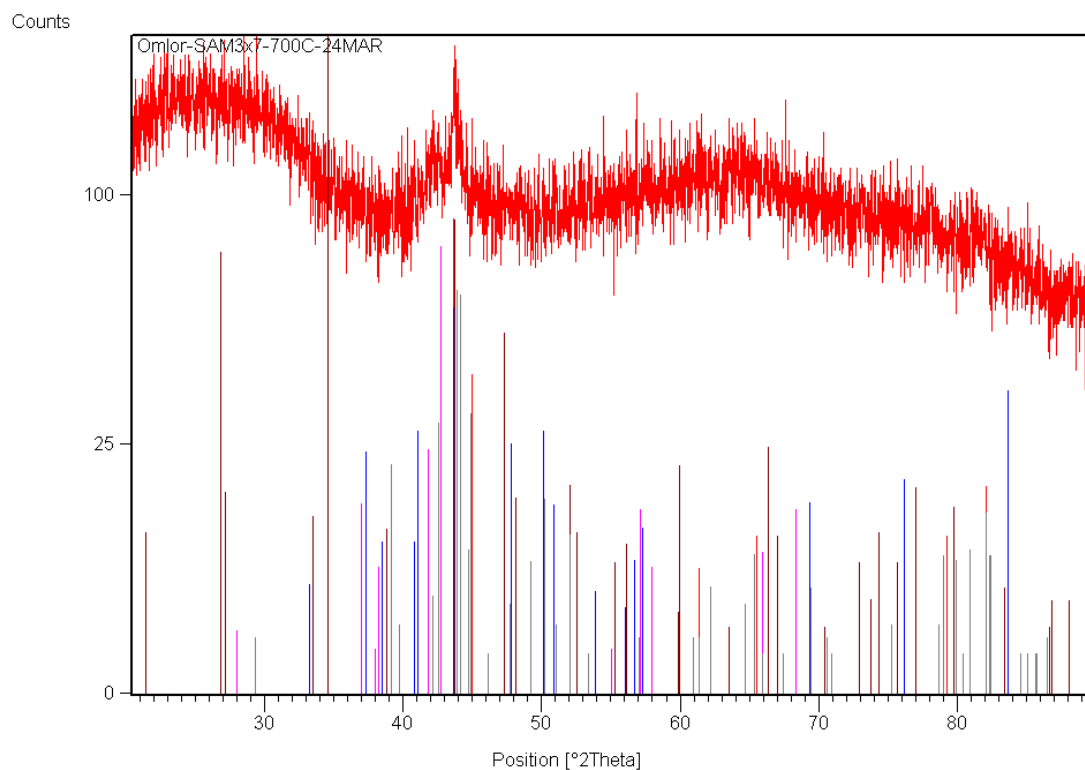


Figure 35. Plot of XRD peaks of possible phases in SAM3X7.

No.	Visi...	Ref. Code	Compoun...	Chemical For...	Score	Scale...	Sem...
1	<input checked="" type="checkbox"/>	00-044-1...	martensite	C0.12 Fe1.88	12	0.521	-
2	<input checked="" type="checkbox"/>	00-026-1...	γ-Mn4 C1.06	Mn4 C1.06	4	0.212	-
3	<input checked="" type="checkbox"/>	00-001-1...	Chromium	Cr	4	0.000	-
4	<input checked="" type="checkbox"/>	00-044-1...	martensite	C0.09 Fe1.91	3	0.376	-
5	<input checked="" type="checkbox"/>	00-011-0...	Silicon Ytr...	Y Si2	0	6.481	-
6	<input checked="" type="checkbox"/>	00-037-0...	Iron Carbide	Fe2 C	2	0.460	-
7	<input checked="" type="checkbox"/>	00-003-1...	Chromium ...	Cr23 C6	1	0.000	-
8	<input checked="" type="checkbox"/>	00-047-1...	Boron Iron	B6 Fe23	4	0.345	-
9	<input checked="" type="checkbox"/>	00-001-1...	Iron	Fe	3	0.000	-
10	<input checked="" type="checkbox"/>	00-036-1...	heptachro...	Cr7 C3	2	0.366	-
11	<input checked="" type="checkbox"/>	00-051-1...	Chromium ...	Cr Si	9	0.518	-
12	<input checked="" type="checkbox"/>	00-001-1...	Chromium	Cr	3	0.000	-

Figure 36. List of possible phases in SAM3X7.



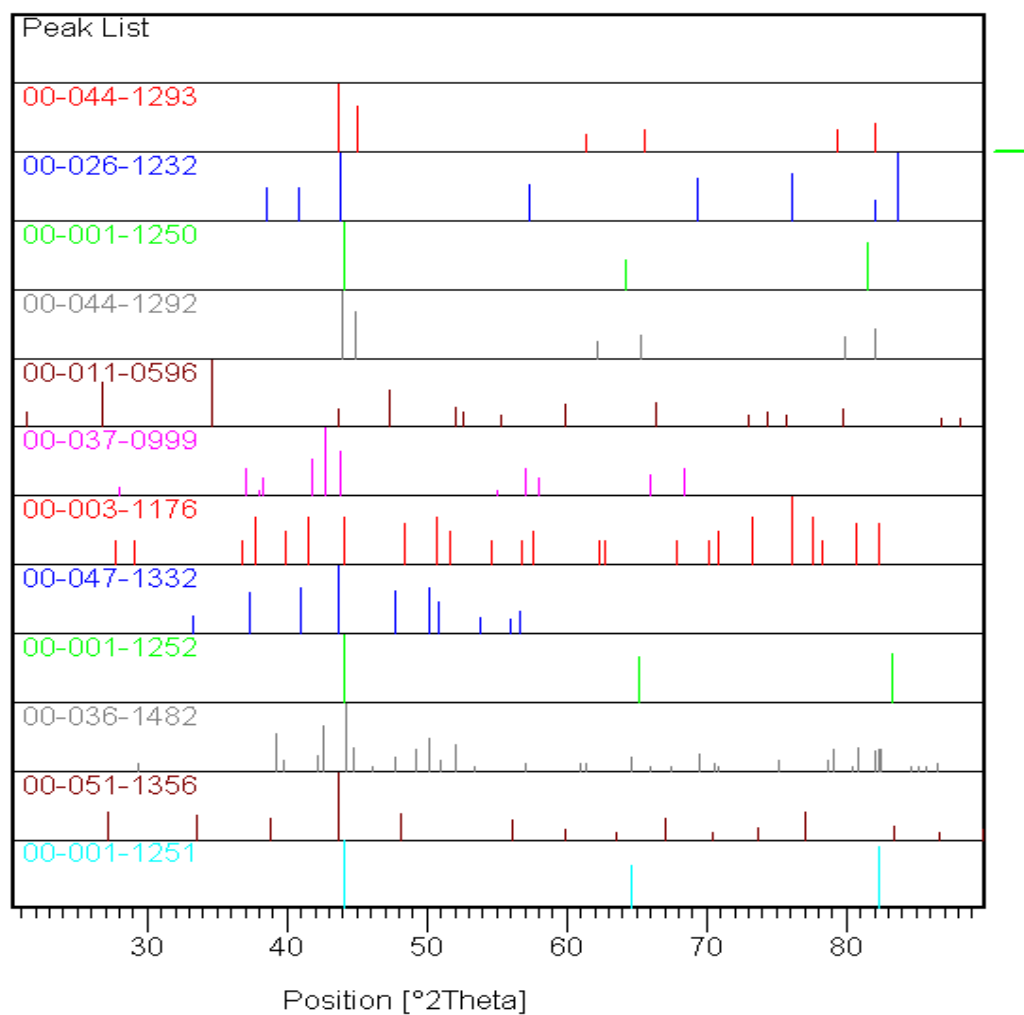


Figure 37. Plot of XRD peaks of possible phases in SAM3X7.

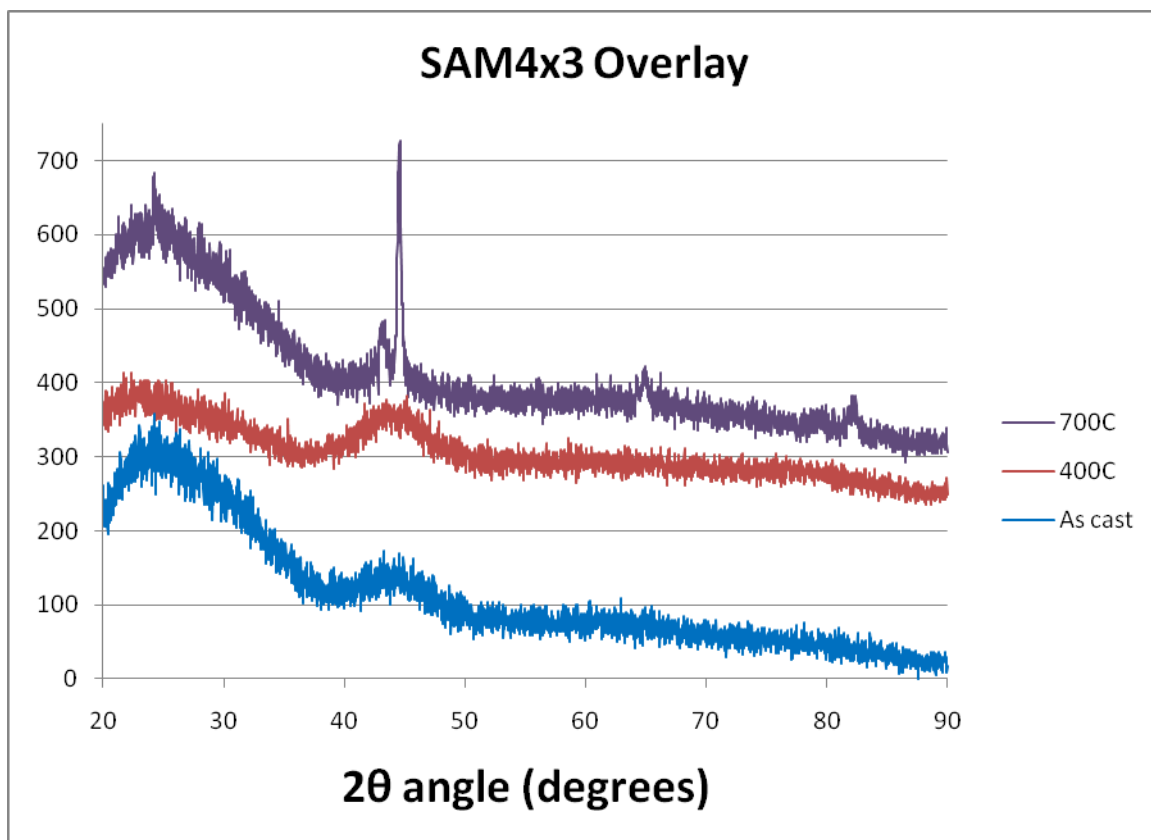


Figure 38. Overlay of SAM4X3 XRD scans as cast, heat treated to 400°C, and heat treated to 700°C.

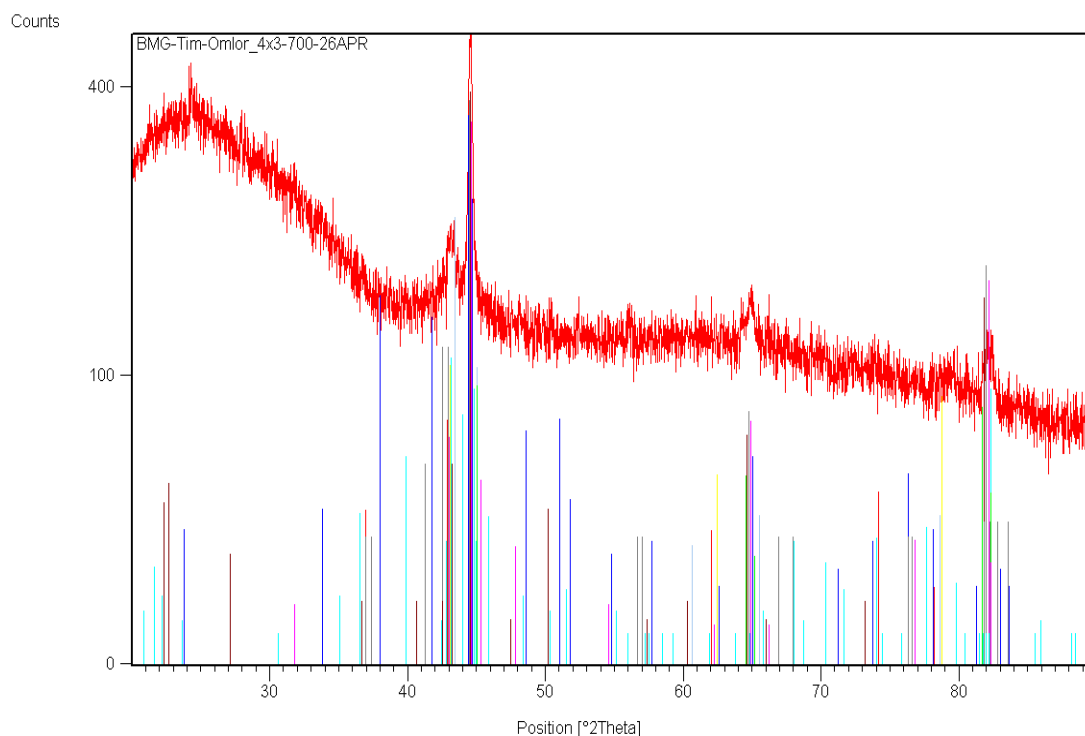


Figure 39. Plot of XRD peaks of possible phases in SAM4X3.

lists Pane							
Pattern List Scan List Peak List Anchor Scan Data Quantification Object Inspector							
Accepted Ref. Pattern: 00-001-1261							
No.	Visi...	Ref. Code	Compound Name	Chemical For...	Score	Scale Factor	Set
1	<input type="checkbox"/>	00-001-1261	Chromium	Cr	42	0.800	
2	<input checked="" type="checkbox"/>	00-006-0696	bainite, ferrite, ledkunitite	Fe	42	0.546	
3	<input checked="" type="checkbox"/>	00-006-0694	Chromium, syn	Cr	38	0.556	
4	<input checked="" type="checkbox"/>	00-034-0396	434-L stainless steel	Fe - Cr	34	0.802	
5	<input checked="" type="checkbox"/>	00-041-1224	Chromium Iron	Cr1.36 Fe0.52	27	0.825	
6	<input checked="" type="checkbox"/>	00-003-1050	Iron	Fe	33	0.191	
7	<input checked="" type="checkbox"/>	00-054-0331	410-L Stainless Steel, ferrite	Fe - Cr	40	0.742	
8	<input checked="" type="checkbox"/>	00-019-0636	Iron Titanium	Fe Ti	12	0.226	
9	<input checked="" type="checkbox"/>	00-020-1316	Tungsten Carbide	W C1-x	11	0.150	
10	<input checked="" type="checkbox"/>	00-028-0646	Manganese Carbide	Mn23 C6	10	0.760	
11	<input checked="" type="checkbox"/>	00-001-1267	Iron	Fe	11	0.195	
12	<input checked="" type="checkbox"/>	00-017-0897	Iron Carbide	Fe2 C	5	0.253	
13	<input checked="" type="checkbox"/>	00-012-0596	Chromium Silicon	Cr Si2	4	0.101	
14	<input checked="" type="checkbox"/>	00-049-1716	Chromium Titanium	Cr2 Ti	3	0.237	
15	<input checked="" type="checkbox"/>	00-001-1234	Manganese	Mn	4	0.130	

Figure 40. List of possible phases in SAM4X3.

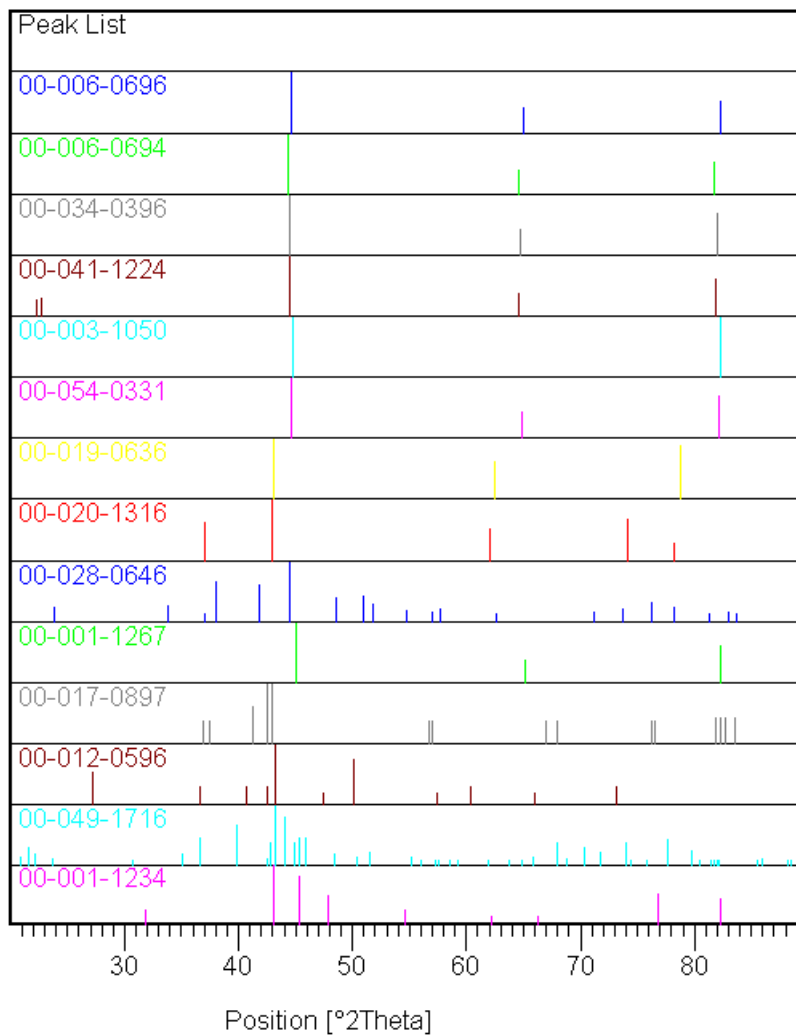


Figure 41. 8. Plot of XRD peaks of possible phases in SAM4X3.

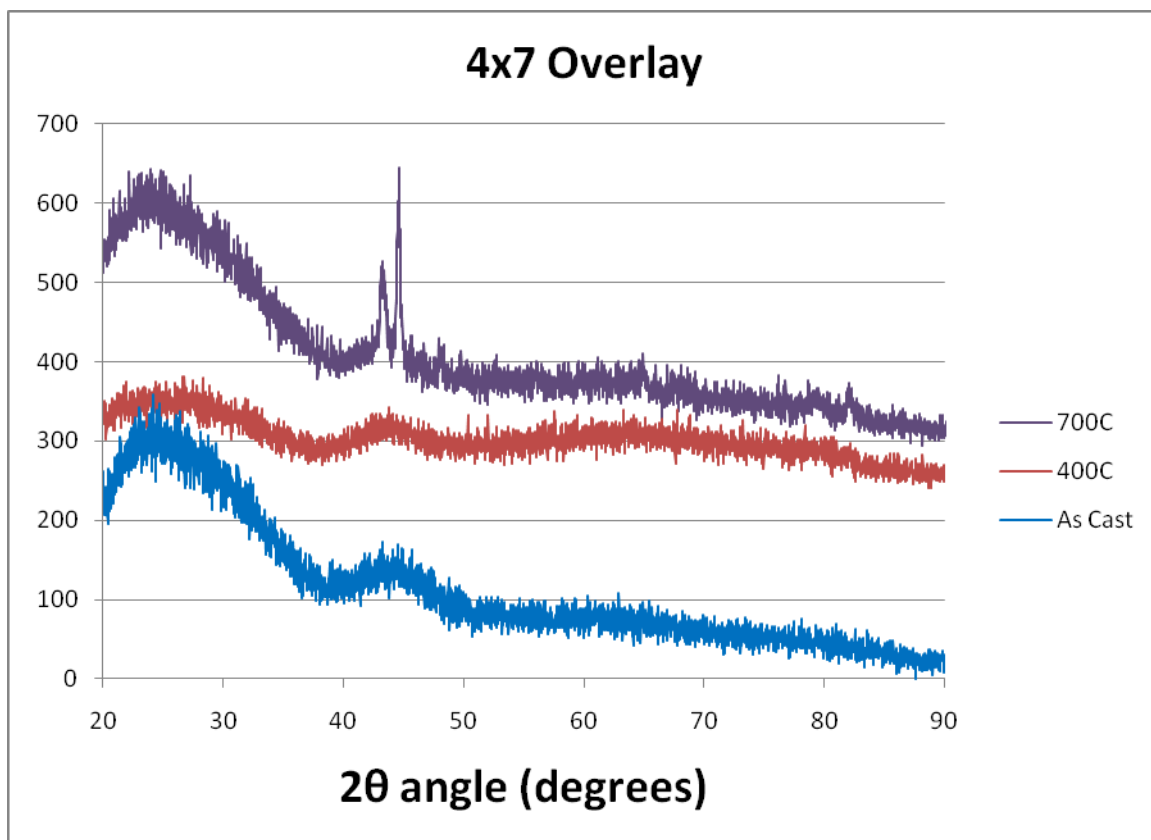


Figure 42. Overlay of SAM4X7 XRD scans as cast, heat treated to 400°C, and heat treated to 700°C.

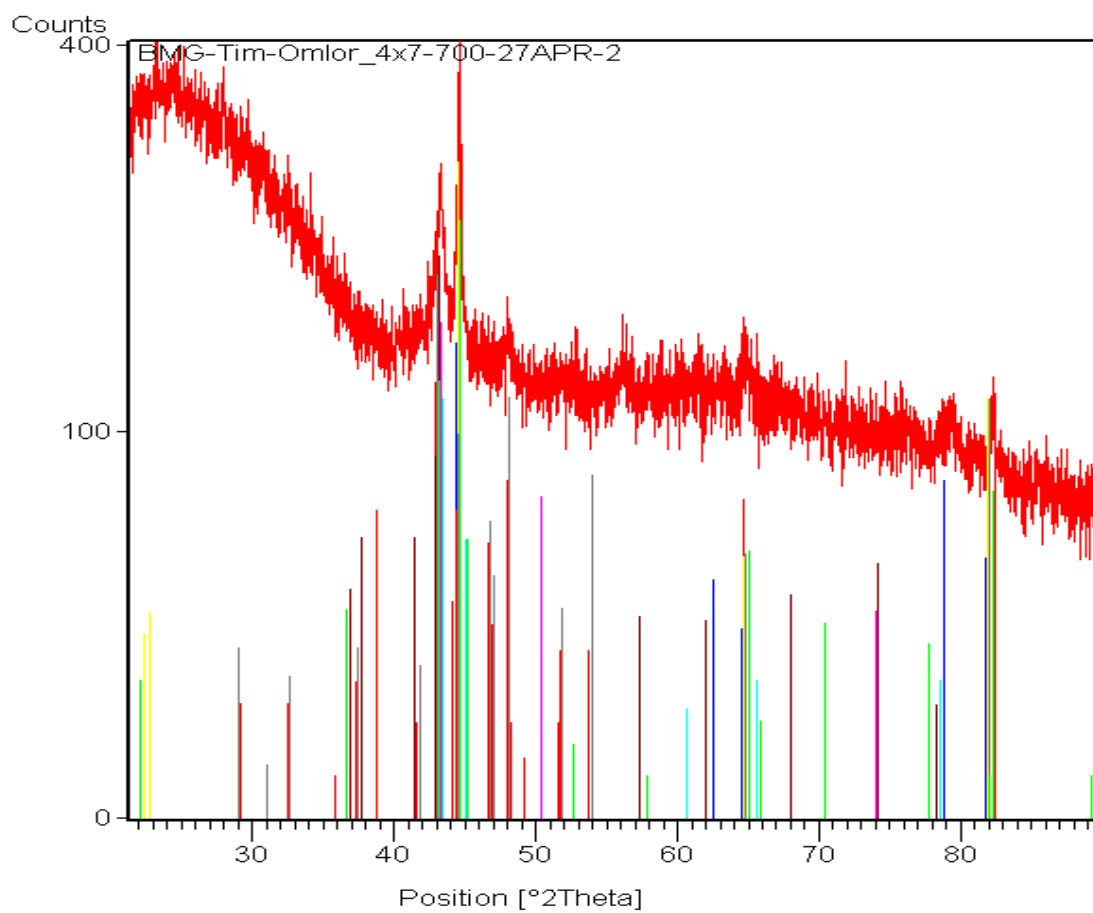


Figure 43. Plot of XRD peaks of possible phases in SAM4X7.

lists Pane

Pattern List

Scan List

Peak List

Anchor Scan Data

Quantification

Object Inspector

Accepted Ref. Pattern: 00-031

Accepted Ref. Pattern: 00-031

Accepted Ref. Pattern: 00-031

No.	Visi...	Ref. Code	Compound N...	Chemical For...	Sc...	Scale Factor	Sem...
1	<input checked="" type="checkbox"/>	00-001-1...	Chromium	Cr	28	1.000	-
2	<input checked="" type="checkbox"/>	00-006-0...	Chromium, syn	Cr	26	0.376	-
3	<input checked="" type="checkbox"/>	00-006-0...	bainite, ferrite, ...	Fe	24	0.593	-
4	<input checked="" type="checkbox"/>	00-034-0...	434-L stainles...	Fe - Cr	23	0.584	-
5	<input checked="" type="checkbox"/>	00-036-1...	Iron Carbide	Fe2 C	19	0.525	-
6	<input checked="" type="checkbox"/>	00-044-1...	martensite	C0.14 Fe1.86	16	0.292	-
7	<input checked="" type="checkbox"/>	00-052-0...	austenite	C Fe15.1	20	0.409	-
8	<input checked="" type="checkbox"/>	00-041-1...	Chromium Iron	Cr1.36 Fe0.52	21	0.712	-
9	<input checked="" type="checkbox"/>	00-039-1...	Boron Iron	Fe3 B	11	0.316	-
10	<input checked="" type="checkbox"/>	00-019-0...	Iron Titanium	Fe Ti	11	0.237	-
11	<input checked="" type="checkbox"/>	00-050-1...	Chromium Tita...	Cr1.97 Ti1.07	13	0.318	-
12	<input checked="" type="checkbox"/>	00-039-1...	Boron Iron	Fe3 B	11	0.489	-
13	<input checked="" type="checkbox"/>	00-020-1...	Tungsten Car...	W C1-x	6	0.218	-
14	<input type="checkbox"/>	00-001-1...	Titanium Carbi...	Ti C	No ...	0.000	-
15	<input type="checkbox"/>	00-002-0...	Titanium Carbi...	Ti C	No ...	0.000	-
16	<input type="checkbox"/>	00-002-0...	Titanium Carbi...	Ti C	No ...	0.000	-
17	<input type="checkbox"/>	00-002-1...	Titanium Carbi...	Ti C	No ...	0.000	-
18	<input type="checkbox"/>	00-003-1...	Titanium Carbi...	Ti C	No ...	0.000	-
19	<input type="checkbox"/>	00-005-0...	Carbon Titaniu...	Ti C	No ...	0.000	-
20	<input type="checkbox"/>	00-006-0...	Titanium Carbi...	Ti C	No ...	0.000	-
21	<input type="checkbox"/>	00-015-0...	Cobalt Silicon ...	Ti Co Si	-	-	-
22	<input type="checkbox"/>	00-031-1...	Khamrabaevit...	Ti C	-	-	-
23	<input type="checkbox"/>	00-032-1...	hongquite	Ti C	-	-	-
24	<input type="checkbox"/>	00-037-1...	Cobalt Titaniu...	Ti Co H1.0	-	-	-
25	<input type="checkbox"/>	00-048-1...	Chromium titan...	C8 H24 O4 S4 ...	-	-	-
26	<input type="checkbox"/>	00-051-0...	Titanium Carbi...	Ti C8	-	-	-
27	<input type="checkbox"/>	00-003-1...	Iron	Fe	-	-	-

Figure 44. List of possible phases in SAM4X7.

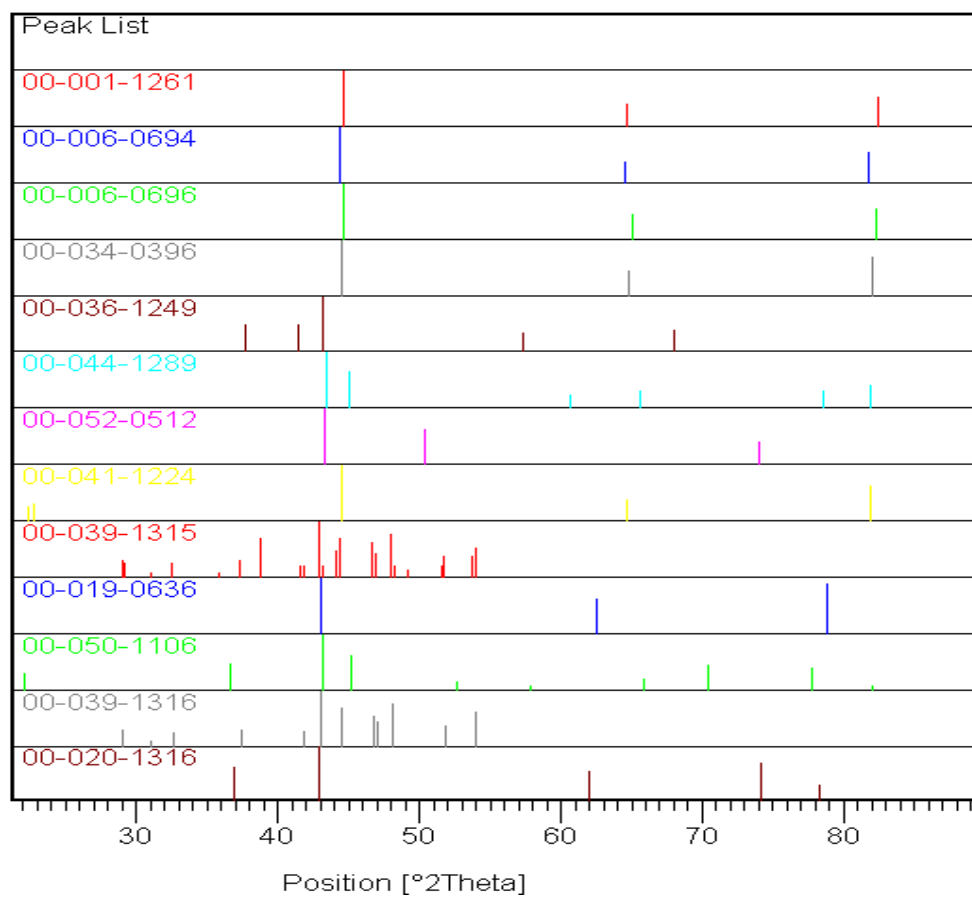


Figure 45. Plot of XRD peaks of possible phases in SAM4X7.



## INITIAL DISTRIBUTION LIST

1. Defense Technical Information Center  
Ft. Belvoir, Virginia
2. Dudley Knox Library  
Naval Postgraduate School  
Monterey, California
3. Joseph Farmer, PhD  
Lawrence Livermore National Laboratory  
Livermore, California
4. Luke Brewer, PhD  
Naval Postgraduate School  
Monterey, California
5. Knox Millsaps, PhD  
Naval Postgraduate School  
Monterey, California
6. Garth Hobson, PhD  
Naval Postgraduate School  
Monterey, California